THE ASTROPHYSICAL JOURNAL, 470:322–335, 1996 October 10

MULTIWAVELENGTH OBSERVATIONS OF SHORT-TIMESCALE VARIABILITY IN NGC 4151. I. ULTRAVIOLET OBSERVATIONS

D. M. CRENSHAW,[1] P. M. RODRÍGUEZ-PASCUAL,[2] S. V. PENTON,[3] R. A. EDELSON,[4] D. ALLOIN,[5] T. R. AYRES,[3] J. CLAVEL,[6] K. HORNE,[7] W. N. JOHNSON,[8] S. KASPI,[9] K. T. KORISTA,[10] G. A. KRISS,[11] J. H. KROLIK,[11] M. A. MALKAN,[12] D. MAOZ,[9] H. NETZER,[9] P. T. O'BRIEN,[13] B. M. PETERSON,[14] G. A. REICHERT,[15] J. M. SHULL,[3,16] M.-H. ULRICH,[17] W. WAMSTEKER,[2] R. S. WARWICK,[18] T. YAQOOB,[19] T. J. BALONEK,[20] P. BARR,[6] G. E. BROMAGE,[21] M. CARINI,[22] T. E. CARONE,[23] F.-Z. CHENG,[24] K. K. CHUVAEV,[25] M. DIETRICH,[26] V. T. DOROSHENKO,[27] D. DULTZIN-HACYAN,[28] A. V. FILIPPENKO,[29] C. M. GASKELL,[30] I. S. GLASS,[31] M. R. GOAD,[32] J. HUTCHINGS,[33] D. KAZANAS,[19] W. KOLLATSCHNY,[34] A. P. KORATKAR,[32] A. LAOR,[35] K. LEIGHLY,[36] V. M. LYUTYI,[37] G. M. MACALPINE,[38] YU. F. MALKOV,[39] P. G. MARTIN,[40] B. MCCOLLUM,[41] N. I. MERKULOVA,[39] L. METIK,[39] V. G. METLOV,[27] H. R. MILLER,[42] S. L. MORRIS,[33] V. L. OKNYANSKIJ,[39,43] J. PENFOLD,[44] E. PÉREZ, G. C. PEROLA,[46] G. PIKE,[19] R. W. POGGE,[14] I. PRONIK,[39] V. I. PRONIK,[39] R. L. PTAK,[47] M. C. RECONDO-GONZÁLEZ,[2] J. M. RODRÍGUEZ-ESPINOZA,[48] E. L. ROKAKI,[49] J. ROLAND,[50] A. C. SADUN,[51] I. SALAMANCA,[5] M. SANTOS-LLEÓ,[5] S. G. SERGEEV,[39] S. M. SMITH,[14] M. A. J. SNIJDERS,[52] L. S. SPARKE,[53] G. M. STIRPE,[54] R. E. STONER,[47] W.-H. SUN,[55] E. VAN GRONINGEN,[43] R. M. WAGNER,[14,56] S. WAGNER,[26] I. WANDERS,[14] W. F. WELSH,[57] R. J. WEYMANN,[58] B. J. WILKES,[59] AND W. ZHENG[11]

Received 1996 February 26; accepted 1996 May 1

ABSTRACT

We present the results of an intensive ultraviolet monitoring campaign on the Seyfert 1 galaxy NGC 4151, as part of an effort to study its short-timescale variability over a broad range in wavelength. The nucleus of NGC 4151 was observed continuously with the *International Ultraviolet Explorer* for 9.3 days, yielding a pair of LWP and SWP spectra every ~70 minutes, and during 4 hr periods for 4 days prior to and 5 days after the continuous-monitoring period. The sampling frequency of the observations is an order of magnitude higher than that of any previous UV monitoring campaign on a Seyfert galaxy.

The continuum fluxes in bands from 1275 to 2688 Å went through four significant and well-defined "events" of duration 2–3 days during the continuous-monitoring period. We find that the amplitudes of the continuum variations decrease with increasing wavelength, which extends a general trend for this and other Seyfert galaxies to smaller timescales (i.e., a few days). The continuum variations in all the UV bands are *simultaneous* to within an accuracy of ~0.15 days, providing a strict constraint on continuum models. The emission-line light curves show only one major event during the continuous monitoring (a slow rise followed by a shallow dip) and do not correlate well with continuum light curves over the short duration of the campaign, because the timescale for continuum variations is apparently smaller than the response times of the emission lines.

Subject headings: galaxies: active — galaxies: individual (NGC 4151) — galaxies: Seyfert — ultraviolet: galaxies

1. INTRODUCTION

Variability monitoring of active galactic nuclei (AGNs) has become a very productive way to probe the spatially unresolved nuclear continuum source and, when present, surrounding broad-line region. The success of recent large-scale monitoring campaigns is due to high temporal sampling rates over extended periods of time (see Peterson 1993 for a review). The cornerstone of most of these campaigns has been the *International Ultraviolet Explorer* (*IUE*) because it can provide long periods of observations at precise intervals, accurate absolute flux levels, and access to the UV, where the continuum and high-ionization lines are more strongly variable than in the optical spectrum. Most campaigns have focused on nearby bright Seyfert 1 galaxies whose UV continua and emission lines were previously known to be strongly variable.

[1] Computer Sciences Corporation, Laboratory for Astronomy and Solar Physics, NASA Goddard Space Flight Center, Code 681, Greenbelt, MD 20771.
[2] ESA *IUE* Observatory, Villafranca, Apdo. Postal 50727, E-28080 Madrid, Spain.
[3] Center for Astrophysics and Space Astronomy, University of Colorado, Campus Box 389, Boulder, CO 80309.
[4] Department of Physics and Astronomy, University of Iowa, Iowa City, IA 52242.
[5] Observatoire de Paris, URA 173 CNRS, F-92195 Meudon, France.
[6] *ISO* Observatory, Astrophysics Division of ESA, ESTEC, Postbus 299, NL-2200 AG Noordwijk, The Netherlands.
[7] School of Physics and Astronomy, University of St. Andrews, North Haugh, St. Andrews KY16 9SS, Scotland.
[8] Naval Research Laboratory, Code 4151, 4555 Overlook Avenue, SW, Washington, DC 20375-5320.
[9] School of Physics and Astronomy and the Wise Observatory, The Raymond and Beverly Sackler Faculty of Exact Sciences, Tel Aviv University, Tel Aviv 69978, Israel.
[10] Department of Physics and Astronomy, University of Kentucky, Lexington, KY 40506-0055.
[11] Department of Physics and Astronomy, Johns Hopkins University, Charles and 34th Streets, Bloomberg Center, Baltimore, MD 21218.
[12] Department of Astronomy, UCLA, Math-Science Building, Los Angeles, CA 90024.
[13] Department of Astrophysics, Oxford University, Keble Road, Oxford OX1 3RH, England.
[14] Department of Astronomy, Ohio State University, 174 W. 18th Avenue, Columbus, OH 43210.

The initial large *IUE* campaign on NGC 5548 is described by Clavel et al. (1991), and results from concurrent and subsequent ground-based monitoring programs are given in Peterson et al. (1991, 1992, 1994) and Dietrich et al. (1993). One of the most fundamental results from these efforts is that there was no detectable delay between the variations in the UV continuum bands and those in the optical; that is, the time lag between the UV and optical light curves was ≤ 4 days. This provides an important constraint on models of the continuum source. For example, for thin accretion disks (see, e.g., Shakura & Sunyaev 1973), this implies that surprisingly high radial signal speeds ($\gtrsim 0.1c$) coordinate the different regions of the disk (Krolik et al. 1991). A possible explanation is that the UV and optical continuum emission is due to reprocessing by cooler, outer material of X-ray photons created closer in (Courvoisier & Clavel 1991; Collin-Souffrin 1991; Krolik et al. 1991).

A major campaign on NGC 3783 with *IUE* (Reichert et al. 1994) and ground-based telescopes (Stirpe et al. 1994) resulted in the same approximate upper limit (≤ 4 days) for the lag between optical and UV continuum variations. A subsequent *Hubble Space Telescope* (*HST*), *IUE*, and ground-based campaign on NGC 5548 (Korista et al. 1995), anchored by daily observations with the Faint Object Spectrograph, demonstrated that the UV and optical continuum variations in NGC 5548 were further constrained to be simultaneous to within ± 1 day. In addition, Clavel et al. (1992) showed that the X-ray and UV continuum fluxes in NGC 5548 are correlated, but with considerable scatter and a rather loose constraint of ≤ 6 days on the time lag. It has become evident that multiwavelength monitoring projects with even higher temporal resolution are needed, in order to obtain tighter constraints on the lags, if any, between X-ray, UV, and optical continuum variations.

The previous campaigns have also demonstrated that the emission-line response times to changes in the photoionizing continuum are very short (days) and a function of ionization, with the high-ionization lines responding more rapidly. In fact, the initial campaigns on NGC 5548 and NGC 3783 (Clavel et al. 1991; Reichert et al. 1994) found that the lags for the highest ionization lines, He II $\lambda 1640$ and N V $\lambda 1240$, were ≤ 4 days. With the higher sampling of the

FOOTNOTES—*Continued*

[15] Universities Space Research Association, NASA Goddard Space Flight Center, Code 668, Greenbelt, MD 20771.
[16] Joint Institute for Laboratory Astrophysics, and National Institute of Standards and Technology, University of Colorado, Campus Box 440, Boulder, CO 80309.
[17] European Southern Observatory, Karl-Schwarzschild-Strasse 2, D-85748 Garching bei München, Germany.
[18] Department of Physics and Astronomy, University of Leicester, University Road, Leicester LE1 7RH, England.
[19] Laboratory for High Energy Astrophysics, NASA Goddard Space Flight Center, Code 665, Greenbelt, MD 20771.
[20] Department of Physics and Astronomy, Colgate University, 13 Oak Drive, Hamilton, NY 13346.
[21] Centre for Astrophysics, University of Central Lancashire, Preston, Lancashire PR1 2HE, England.
[22] Center for Automated Space Studies, Department of Physics and Astronomy, Western Kentucky University, 1526 Russellville Road, Bowling Green, KY 42101-3576.
[23] Space Sciences Laboratory, University of California, Berkeley, Berkeley, CA 94720, and Eureka Scientific, Inc.
[24] Center for Astrophysics, University of Science and Technology of China, 96 Jinzai lu, Hefei, Anhui 230026, China.
[25] Deceased, 1994 November 15.
[26] Landessternwarte Königstuhl, D-69117 Heidelberg, Germany.
[27] Sternberg State Astronomical Institute, P/O Nauchny, 334413 Crimea, Ukraine.
[28] Instituto de Astronomía, Universidad Nacional Autónoma de México, Apdo. Postal 70-264, 04510 México D.F., Mexico.
[29] Department of Astronomy, University of California, Berkeley, Berkeley, CA 94720.
[30] Department of Physics and Astronomy, University of Nebraska, Lincoln, NE 68588-0111.
[31] South African Astronomical Observatory, P.O. Box 9, Observatory 7935, South Africa.
[32] Space Telescope Science Institute, 3700 San Martin Drive, Baltimore, MD 21218.
[33] Dominion Astrophysical Observatory, 5071 W. Saanich Road, Victoria, BC V8X 4M6, Canada.
[34] Universitäts-Sternwarte Göttingen, Geismarlandstrasse 11, D-37083 Göttingen, Germany.
[35] Department of Astronomy, California Institute of Technology, 130-33, Pasadena, CA 91125.
[36] Cosmic Radiation Laboratory, RIKEN, Hirosawa 2-1, Wako, Saitama 351-01, Japan.
[37] Sternberg Astronomical Institute, University of Moscow, Universitetskij Prospect 13, 119899 Moscow, Russia.
[38] Department of Astronomy, University of Michigan, 830 Dennison, Ann Arbor, MI 48109-1090.
[39] Crimean Astrophysical Observatory, P/O Nauchny, 334413 Crimea, Ukraine.
[40] Canadian Institute for Theoretical Astrophysics, University of Toronto, 60 St. George Street, Toronto, ON M5S 1A1, Canada.
[41] Computer Sciences Corporation, NASA Goddard Space Flight Center, Code 684.9, Greenbelt, MD 20771.
[42] Department of Physics and Astronomy, Georgia State University, Atlanta, GA 30303.
[43] Astronomiska observatoriet, Box 515, S-751 20 Uppsala, Sweden.
[44] Department of Physics and Astronomy, University of Calgary, 2500 University Drive, NW, Calgary, AB T2N 1N4, Canada, and Department of Mathematics, Physics, and Engineering, Mount Royal College, Calgary, AB T3E 6K6, Canada.
[45] Instituto de Astrofísica de Andalucía, Apdo. Correos 3004, E-18080 Granada, Spain.
[46] Istituto Astronomico dell'Università, via Lancisi 29, I-00161 Roma, Italy.
[47] Department of Physics and Astronomy, Bowling Green State University, Bowling Green, OH 43403.
[48] Instituto de Astrofísica de Canarias, Via Lactea, E-38200 La Laguna, Tenerife, Spain.
[49] Royal Observatory Edinburgh, University of Edinburgh, Blackford Hill, Edinburgh EH9 3HJ, Scotland.
[50] Institut d'Astrophysique, 98 bis, Boulevard Arago, F-75014 Paris, France.
[51] Department of Physics and Astronomy and Bradley Observatory, Agnes Scott College, Decatur, GA 30030.
[52] Institut de Radio Astronomie Millimétrique, 300 Rue de la Piscine, F-38046 St. Martin d'Hères, France.
[53] Department of Astronomy, University of Wisconsin, 475 N. Charter Street, Madison, WI 53706.
[54] Osservatorio Astronomico di Bologna, via Zamboni 33, I-40126, Bologna, Italy.
[55] Institute of Astronomy, National Central University, Chung-Li, 32054, Taiwan.
[56] Postal address: Lowell Observatory, 1400 W. Mars Hill Road, Flagstaff, AZ 86001.
[57] Department of Physics, Keele University, Keele, Staffordshire ST5 5BG, England.
[58] Observatories of the Carnegie Institution of Washington, 813 Santa Barbara Street, Pasadena, CA 91101.
[59] Harvard-Smithsonian Center for Astrophysics, 60 Garden Street, Cambridge, MA 02138.

subsequent *HST*, *IUE*, and ground-based campaign on NGC 5548, Korista et al. (1995) were able to determine that the lags for these lines were slightly less than 2 days. Thus another reason for obtaining higher temporal resolution is to check this result for this and other Seyfert galaxies and, specifically, to fully resolve the transfer function of the high-ionization lines (Peterson 1993).

We report on a new campaign to provide an order-of-magnitude increase in the sampling rate over previous campaigns on Seyfert 1 galaxies, similar to that obtained for the BL Lacertae object PKS 2155−304, which was monitored continuously by *IUE* for 5 days (Urry et al. 1993) as part of a multiwavelength campaign (Edelson et al. 1995). We also made a determined effort to obtain concurrent observations of NGC 4151 at other wavelengths, particularly in the optical and X-ray regions, to test the predictions of accretion disk and continuum reprocessing models. This would also allow a comparison with the multiwavelength observations of PKS 2155−304, an object with a strong *beamed* component. The data and basic results from the *IUE* campaign on NGC 4151 are given in this paper. Other papers in this series report optical observations (Kaspi et al. 1996, hereafter Paper II), high-energy observations (Warwick et al. 1996, hereafter Paper III), and a comparison of the multiwavelength continuum data (Edelson et al. 1996, hereafter Paper IV).

NGC 4151 is a nearby ($cz = 995$ km s^{-1}) barred spiral galaxy that is viewed nearly face-on (Simkin 1975). It was classified as Seyfert 1.5 by Osterbrock & Koski (1976) because its nucleus shows strong narrow components for the permitted lines in addition to the broad (thousands of km s^{-1} FWHM) permitted and narrow (hundreds of km s^{-1} FWHM) forbidden lines that define a Seyfert 1 galaxy. *HST* images show that the narrow-line [O III] λ5007 emission arises from a nuclear point source and an extended ($\sim 3''$) narrow-line region that consists of a number of emission-line clouds in a biconical structure (Evans et al. 1993). The radio emission is extended along the same general direction as the [O III] emission on arcsecond and subarcsecond scales (Johnston et al. 1982; Wilson & Ulvestad 1982), although the optical emission-line and radio axes are misaligned by $\sim 20°$. NGC 4151 exhibits a complex X-ray spectrum, which can be characterized in the 2–10 keV region by a power-law continuum modified by a warm or partial absorber and a soft X-ray excess in the 0.1–2 keV range (Holt et al. 1980; Yaqoob, Warwick, & Pounds 1989; Weaver et al. 1994a, 1994b).

Because it is so bright and strongly variable in the UV, NGC 4151 is an ideal target for intensive monitoring (see Ulrich et al. 1991 for a summary of previous UV observations). It shows UV continuum variations with doubling times as small as a week (Clavel et al. 1990) and is one of the small number of AGNs for which emission-line lags have been reliably determined by cross-correlation of the emission and continuum light curves. The most accurate lags determined for NGC 4151 thus far are 4 ± 3 days for C IV λ1549 (Clavel et al. 1990) and 9 ± 2 days for the Balmer lines (Maoz et al. 1991), confirming earlier estimates by Gaskell & Sparke (1986) and Peterson & Cota (1988). The UV spectrum of NGC 4151 shows extremely broad emission lines ($\sim 30{,}000$ km s^{-1} FWZI for C IV). It also contains a number of broad (1000 km s^{-1}), blueshifted (-1100 to -100 km s^{-1}), and variable absorption lines that arise in ions of widely different stages (Bromage et al. 1985; Kriss et al. 1992) and two unidentified emission lines, known as L1 λ1518 and L2 λ1594, that bracket the C IV λ1549 feature (Ulrich et al. 1985; Clavel et al. 1987).

2. OBSERVATIONS

The nucleus of NGC 4151 was observed with the *IUE* SWP (1150–1970 Å) and LWP (1970–3300 Å) cameras through the large apertures ($10'' \times 20''$) in low-dispersion mode (resolution = 5–8 Å FWHM). Observations were made in a continuous mode over 9.3 days during 1993 December 1–10. In addition, observations were obtained during 4 hr US 2 shifts (which frequently experience higher particle radiation) on the 4 days prior to and 5 days after the continuous-monitoring period. The standard observing procedure was to obtain alternate LWP and SWP exposures by reading and preparing one camera while the other camera was exposing, which resulted in a pair of spectra every ~ 70 minutes. Typical exposure times were 20 minutes for the SWP images and 10 minutes for the LWP images. During each day of the continuous monitoring, the observations were interrupted for ~ 2 hr as Earth occulted the target, and the spacecraft was maneuvered to a low β (angle between the telescope axis and the antisolar direction) to maintain attitude control and cool the on-board computer.

The observations were affected by the presence of scattered solar (and occasionally Earth) light in the telescope tube, which has been present since early 1991 and is strong at $\beta \geq 50°$ (Carini & Weinstein 1992). In order to obtain concurrent observations with other satellites (e.g., *ROSAT*), it was necessary to observe NGC 4151 at $\beta \approx 90°$. The scattered light's spectrum is such that there is contamination of the LWP spectra at the long-wavelength end (see § 3.2) but no contamination of the SWP spectra. The most notable effect of the scattered light is that it greatly increases the background level in the fine-error sensor (FES), which is the optical target-acquisition detector. Thus the nucleus of NGC 4151 could not be detected directly, since the FES background counts exceeded those expected for the target by a factor of ~ 50, and no optical light curve could be obtained from the FES. Fortunately, the scattered light had little effect on acquisition and guiding during the exposures. The nucleus of NGC 4151 was acquired by blind offset from a nearby bright star (SAO 62869), which is a procedure that typically results in a positioning error in the aperture that is less than $1''$. During the exposures, the same bright star was used for guiding since it remained in the portion of the FES field of view that is least affected by the scattered light. The offset slew was repeated about once every 8 hr to recenter the target in the aperture and to update the guide star's position since the spacecraft rolls to maintain optimal positioning of the solar arrays.

The details of individual observations can be obtained from the *IUE* Merged Log, which is available through the *IUE* data analysis centers at NASA Goddard Space Flight Center and the ESA Villafranca Satellite Tracking Station (VILSPA); the program IDs for these observations are "IMPRE" (NASA) and "QQ105" (VILSPA). For example, there was significant particle radiation for some of the images obtained during the US 2 shifts, which could result in slightly lower signal-to-noise ratios for the affected spectra. These spectra can be identified in the Merged Log from background levels that are higher than the average background levels, which are typically ~ 15 DN (data numbers) for the SWP and ~ 27 DN for the LWP.

A total of 205 SWP and 196 LWP spectra were obtained of NGC 4151 during the campaign. Only six images are considered to be unusable. The exposure time for SWP 49394 was cut short because of an impending Earth occultation. The target was on the edge of the aperture for LWP 26984, SWP 49428, and LWP 26895. Most of the two images for LWP 26931 and LWP 27008 were lost as a result of telemetry problems and could not be recovered. The other problems encountered are minor and do not significantly affect the measured fluxes. We are left with 395 useful spectra to work with: 203 SWP and 192 LWP.

3. DATA REDUCTION AND ANALYSIS

The *IUE* project has developed techniques for improving the signal-to-noise ratio, wavelength assignment, and flux calibration of *IUE* spectra; these techniques are being used in the new processing system (NEWSIPS) to produce the *IUE* Final Archive. However, at the time of the observations, only the old processing system (IUESIPS) was available for current data. We decided to use a newly available system developed by T. Ayres, called "TOMSIPS."

3.1. *TOMSIPS Reduction*

TOMSIPS is based on many of the techniques developed for NEWSIPS and includes a realistic noise model (Ayres 1993). TOMSIPS, like NEWSIPS, uses an identically rotated intensity transfer function (ITF). The old IUESIPS used prerotated ITFs, which do not always match up with the current image and can introduce fixed pattern noise. TOMSIPS uses an ITF based directly on the raw images of the flux-standard white dwarf G191B2B and a wavelength calibration based upon the emission-line spectra of λ Andromeda.

TOMSIPS uses a slit-weighted extraction method similar to the OPTIMAL technique (see Kinney, Bohlin, & Neill 1991), with the distinct difference that the cross-dispersion profile is not of a fixed form but matches the actual average cross-dispersion profile in the region. Because the cross-dispersion profile is both wavelength and emission-line dependent, 10 separate cross-dispersion regions are used for the SWP and seven are used for the LWP. Unlike previous extraction techniques, including OPTIMAL and GEX (Gaussian extraction; see Reichert et al. 1994), the TOMSIPS errors are not "extraction" errors but are true estimates of the flux uncertainties empirically derived from an independent noise model (Ayres 1993). The improved noise model and similarly processed ITF substantially reduce the pixel-to-pixel variations of the final spectra. A detailed comparison of TOMSIPS with other processing techniques appears in Penton et al. (1996).

3.2. *Scattered-Light Contamination of LWP Spectra*

The scattered light in the *IUE* telescope is characterized by a solar spectrum (Carini & Weinstein 1992) and therefore rises sharply at the long-wavelength end of the LWP region. Unfortunately, the scattered light exhibits a strong (and possibly variable) gradient across the aperture, and there are no proven techniques for removing it at this time. The flux levels of several sky-background LWP spectra obtained during the campaign indicate that the scattered light contributed the following approximate percentages to the total fluxes in the continuum bands: ~1% at 2300 Å, ~7% at 2688 Å, ~26% at 2970 Å, and ~37% at 3130 Å. Checks of the flux levels inside the aperture, but away from the spectra, indicate that the background contribution varied by $\leq 1\%$ at 2688 Å over the course of the campaign. At longer wavelengths, the background variation started to significantly alter the observed continuum variations.

3.3. *Continuum and Line Measurements*

Continuum measurements were made in known line-free bands in the rest frame of NGC 4151. A continuum flux is taken to be the error-weighted mean over the bandpass, and the continuum flux error is the standard deviation of the mean over the bandpass. For SWP spectra, the continuum regions selected are 1260–1290, 1420–1460, and 1805–1835 Å. In the LWP spectra, the only usable continuum band is 2625–2750 Å; at shorter wavelengths, the spectra are too noisy, and at longer wavelengths, the spectra are too contaminated by the variable scattered light. The continuum bands are shown in Figure 1, along with the average SWP and LWP spectra for this campaign. The sharp upturn at the long-wavelength end is due to the scattered-light contamination.

To measure the emission- and absorption-line components, predefined regions around each feature of interest are extracted, and a fit is made in the rest frame. Initially, the fit consists of a power-law continuum of the form $F_\lambda = F_0(\lambda/\lambda_0)^\alpha$, with the data weighted by the TOMSIPS errors. Gaussian components of the form

$$F_\lambda^G = F_0 \exp\left[-\frac{(\lambda - \lambda_c)^2}{2\sigma_G^2}\right] \quad (1)$$

are added to measure the emission and absorption features. The Gaussians are initially centered at the expected line center (λ_c) but are allowed to "float" in wavelength (λ), width (σ_G), and amplitude (F_0). The float in wavelength and width is required to compensate for wavelength calibration errors and the asymmetry of the broad emission lines. All Gaussian components without an initially fixed minimum width are constrained to have a minimum width of twice the instrumental profile ($\sigma_G = 1.5$ Å) to prevent fitting of spurious pixels. Five separate regions containing emission features, absorption features, or both were examined separately since slightly different procedures are needed to properly fit each spectral feature. These regions are 1155–1315 Å (Lyα and N v λ1240), 1307–1463 Å (C II λ1334, Si IV

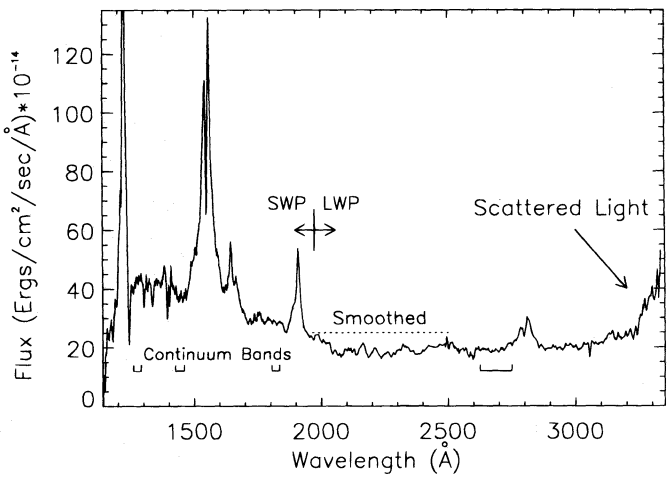

FIG. 1.—Averaged and combined SWP and LWP spectrum of NGC 4151 for the 1993 campaign. The 1975–2500 Å region has been smoothed with a 10 pixel (~15 Å) boxcar filter for display purposes.

λ1398, and O IV] λ1402), 1425–1750 Å (N IV] λ1486, C IV λ1549, He II λ1640, and O III] λ1663), 1790–1960 Å (Al III λ1857, Si III] λ1890, and C III] λ1909), and 2640–2915 Å (Mg II λ2800).

To ensure an unbiased extraction of the parameters characterizing the UV emission and absorption features, the spectral components are systematically fitted with a modified version of the MINUIT (James & Roos 1975) software. The CERN-developed MINUIT uses the nonlinear least-squares Levenberg-Marquart method to fit χ^2-minimizing Gaussian components to the spectral features. Errors in the fitting parameters are determined by exploring parameter space near the minimum and are reported as 1 σ errors.

Complicated features such as C IV require multiple Gaussian components. While each new component will reduce χ^2, it may not always be statistically significant. In these cases, an F-test is applied (see Bevington 1969, p. 200). Only when the component passes the F-test will it be added to the final fit. As an additional restriction, we have chosen to limit the maximum number of components for each specific line (e.g., C IV λ1549) to three. All Gaussians were initially allowed a wide range of parameter space to achieve the best fit; this range was reduced as obvious trends in the fits became apparent.

Line fluxes were calculated by integrating and adding together the individual components of the feature of interest. A quadrature sum of the individual integrated Gaussian errors is not a true error estimate of the integrated flux but in fact overestimates the true error. Similar to a method used in a previous campaign on NGC 5548 (Clavel et al. 1991), the point-to-point integrated light-curve variations were used to scale the errors to the proper values.

Table 1 shows the allowed ranges and means of the final component fits. The components that were summed together to produce a measurement for a particular line or blend are described in § 3.4. Figure 2 shows an example of the combined fit to an individual SWP spectrum.

3.4. *Summation of Line Components*

We attach no physical significance to individual components for a particular line (e.g., C IV λ1549); the component fits are just a convenient description of the data. In addition, many of the individual emission and absorption lines in a given region are blended as a result of their proximity, and their individual light curves are noisy and difficult to interpret as a result of the fitting technique's inability to accurately deconvolve them. Therefore, as in the past (Clavel et al. 1991; Reichert et al. 1994), we use the sum of components to represent the dominant emission line in a particular region. When we quote results for a particular sum of components, we use the dominant emission feature as a designation (e.g., "C IV" for the sum of the components of C IV and N IV]).

Many of the features in NGC 4151 are very difficult to measure accurately because of contamination, the complicated nature of the UV spectrum (many broad and narrow emission and absorption lines), or both. Their light curves at relatively low levels of variability are very noisy and cannot be used for the detailed analyses in § 4. The redshift of NGC 4151 places its Lyα emission at 1219.7 Å, which is too close to the geocoronal emission to allow a separate fit to the two narrow components. Hence the Lyα+N V light curve is dominated by the substantial variation of geocoronal Lyα over the course of each day and is not usable for this study. As shown in Table 1, the Si IV+O IV] feature is dominated by a strong Si IV absorption doublet, and an accurate measurement of the intrinsic emission is not possible. Finally, the Mg II feature is strongly affected by the scattered light, particularly in the red wing.

The fluxes of the features around C IV, He II, and C III] can be measured accurately enough to produce reasonably good light curves. The C IV line profile is complicated, showing multicomponent emission and self-absorption. Because of their proximity, the C IV, N IV], He II, and O III]

TABLE 1

GAUSSIAN COMPONENTS—RANGES, MEANS, AND STANDARD DEVIATIONS

	F_0 (10^{-14} ergs s^{-1} cm^{-2} Å^{-1})			λ_c (Å)			σ_G (Å)		
FITTED COMPONENT	Min	Mean	Max	Min	Mean	Max	Min	Mean	Max
Lyα:									
Absorption	−212.9	−112.0 ± 30.6	−51.5	1211.0	1215.5 ± 1.9	1220.0	1.8	4.4 ± 1.3	8.0
Narrow	95.2	164.0 ± 29.5	270.5	1212.8	1217.5 ± 1.3	1220.2	2.1	3.4 ± 0.4	4.5
Broad	59.6	87.6 ± 19.0	172.5	1216.1	1219.9 ± 1.3	1222.0	8.7	12.6 ± 1.5	15.5
N V	−60.0	−44.4 ± 8.8	−20.1	1236.0	1238.1 ± 1.0	1240.0	2.6	3.9 ± 0.4	5.0
C II absorption	−14.7	−9.3 ± 2.1	−5.5	1327.0	1330.7 ± 1.3	1333.6	1.5	2.9 ± 0.7	5.0
Si IV:									
Absorption 1	−32.5	−23.5 ± 3.8	−14.2	1387.0	1389.5 ± 0.9	1392.0	1.7	3.1 ± 0.6	4.1
Absorption 2	−23.9	−15.7 ± 3.0	−5.8	1396.0	1398.4 ± 0.8	1401.0	1.3	2.1 ± 0.3	3.0
Si IV+O IV] emission	6.0	12.6 ± 3.9	17.5	1388.0	1390.3 ± 1.8	1395.5	6.0	12.0 ± 2.6	16.0
N IV]	2.0	6.2 ± 1.9	11.5	1480.0	1486.1 ± 3.1	1491.0	0.7	6.6 ± 2.5	9.0
C IV:									
Absorption	−110.0	−89.6 ± 8.8	−70.0	1543.0	1544.9 ± 0.9	1547.0	2.7	3.3 ± 0.2	4.0
Narrow	62.8	78.2 ± 7.7	99.6	1544.0	1545.8 ± 0.8	1547.7	7.5	9.7 ± 1.1	12.0
Broad	23.8	38.7 ± 3.8	50.5	1543.0	1546.1 ± 1.6	1551.0	27.5	34.5 ± 2.1	36.5
He II	16.0	19.8 ± 1.9	25.7	1636.0	1638.1 ± 1.0	1640.0	4.5	8.4 ± 1.7	10.5
O III]	7.0	10.8 ± 1.5	14.5	1657.4	1662.8 ± 2.0	1666.0	4.5	8.9 ± 1.0	9.5
Al III] absorption	−5.0	−2.6 ± 1.0	0.0	1848.0	1854.1 ± 3.3	1860.0	0.0	4.6 ± 1.9	8.0
Si III]	4.0	7.3 ± 1.7	10.5	1879.0	1884.2 ± 2.8	1890.0	3.9	9.9 ± 1.2	10.5
C III]:									
Narrow	13.9	21.0 ± 3.0	28.3	1901.0	1903.4 ± 1.0	1905.8	3.3	4.9 ± 0.5	6.1
Broad	3.0	6.6 ± 2.8	12.0	1903.0	1907.3 ± 4.7	1919.0	7.0	13.3 ± 3.0	17.0
Red	1.0	3.8 ± 1.5	8.0	1912.0	1915.0 ± 1.1	1918.0	0.7	2.5 ± 0.9	4.7

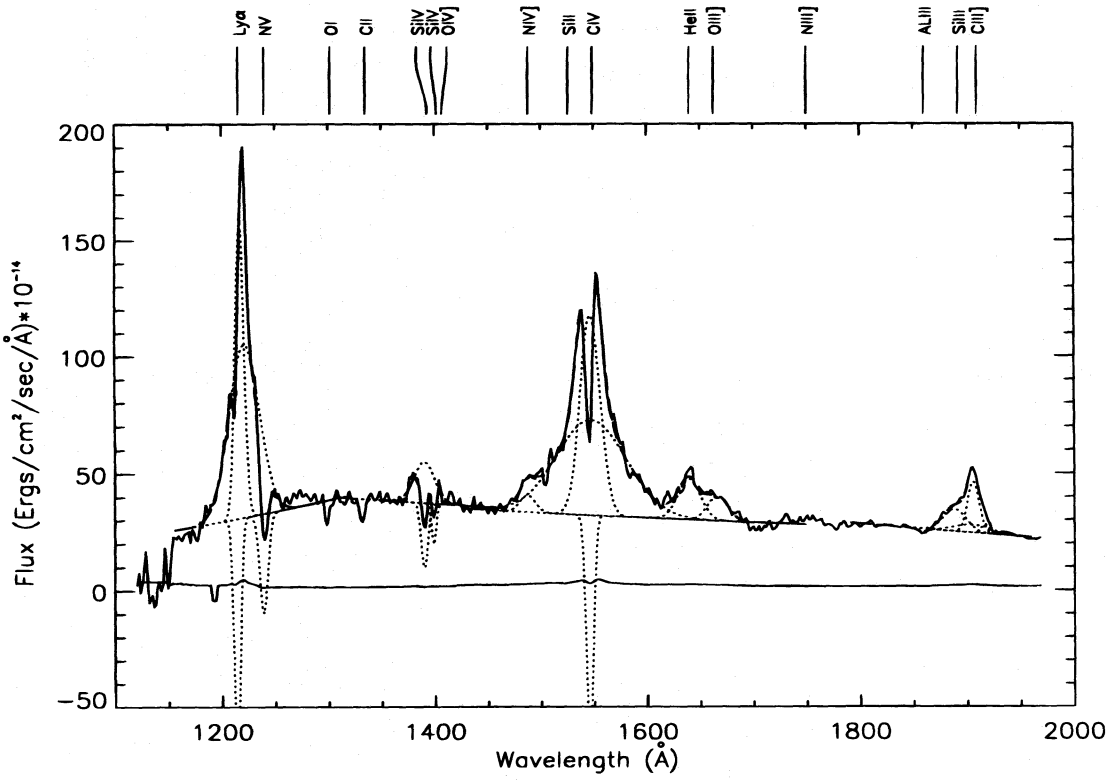

FIG. 2.—Sample spectrum (SWP 49555) and spectral fits. The solid line is the observed spectrum, the dotted lines are the spectral components, and the dot-dashed line is the sum of the components.

features are all fitted simultaneously. The N IV], O III], and He II features are each fitted with a single Gaussian, while the more complicated C IV feature is fitted with three Gaussian components: a narrow emission component, a very narrow absorption component, and an extended emission component. The He II and O III] emissions are blended but distinct enough from the C IV emission to be treated as a separate feature. Thus we have separate measurements for C IV + N IV] and He II + O III].

The C III] region is modeled with an absorption component for Al III, a single emission component for Si III], and up to three emission components for C III], as shown in Table 1. Because of the asymmetry of the C III] emission, three components are needed: a narrow component, a broad component, and a component labeled "red." The red component is limited in central wavelength to avoid interference with the Si III] emission on the blue wing of C III]. The Al III absorption on the extreme blue wing of the emission can be separated from the overall feature, so the measurement is for C III] + Si III].

3.5. *Comparison with IUESIPS*

As a consistency check on the TOMSIPS processing scheme, we compared the measured continuum fluxes with those obtained in the same wavelength bins from the IUESIPS spectra. Figure 3 shows this comparison for the 1275 Å bin, demonstrating that the fluxes from the two methods are extremely well correlated (the linear correlation coefficient is $r = 0.96$). The other SWP continuum bins show the same excellent correlation, with the TOMSIPS fluxes systematically higher than the IUESIPS fluxes by 1%–10%, depending on the bin. This is a direct consequence of the slightly different (and improved) photometric correction and absolute-sensitivity calibration as a function of wavelength.

3.6. *Effects of Reddening*

In principle, the effects of reddening by dust on the intrinsic continuum and emission-line fluxes can be very significant. However, we note that our principal results are on the

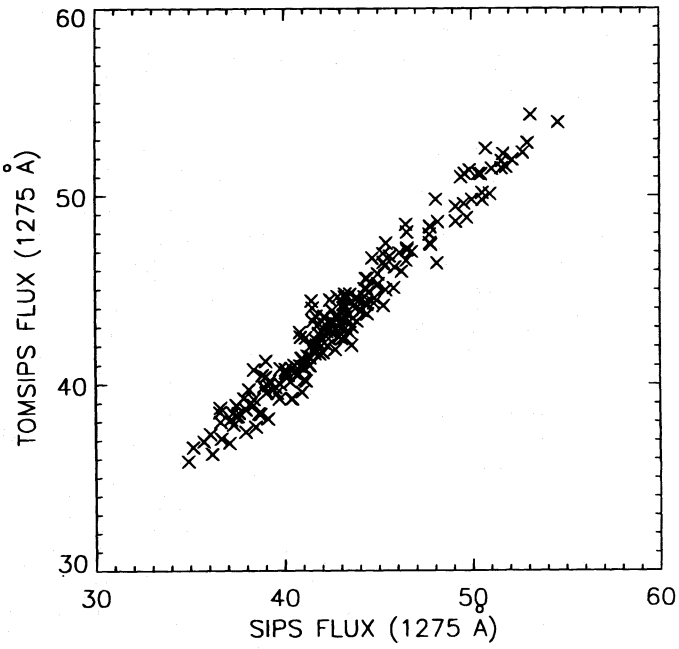

FIG. 3.—Continuum fluxes in the 1275 Å band. Fluxes from TOMSIPS are plotted as a function of those from IUESIPS in units of 10^{-14} ergs s^{-1} cm^{-2} $Å^{-1}$.

fractional amplitudes and timescales of the variations, which are not affected by reddening. In addition, a variety of estimates indicate that reddening is quite weak in NGC 4151. The Galactic reddening is essentially zero: the H I column density of 2.1×10^{20} cm^{-2} (Stark et al. 1992) yields $E_{B-V} \leq 0.01$ (according to Burstein & Heiles 1982). Penston et al. (1981) show that the *total* reddening of the UV continuum determined from the 2200 Å feature is $E_{B-V} \leq 0.1$; we have verified this result by using the average NGC 4151 spectrum for this campaign and by assuming that the interstellar extinction curve of Savage & Mathis (1979) is applicable. Kriss et al. (1992) calculated $E_{B-V} = 0.039$ from a power-law plus Galactic extinction fit to the far-UV spectrum of NGC 4151. For the narrow emission lines, Kriss et al. (1992) determined that $E_{B-V} \leq 0.12$ from the recombination lines He II λ1085 and He II λ1640. There is currently no accurate way to determine the reddening of the broad components of the lines, although it is not expected that dust could survive in the broad-line region of NGC 4151 (Ferland & Mushotzky 1982).

4. RESULTS

Tables 2 and 3 list the TOMSIPS continuum and line fluxes (and associated errors) as a function of Julian Date at the *midpoint* of the SWP and LWP exposures. The image numbers are given so that data points can be identified with specific images. The few observations of NGC 4151 that are not included in these tables are listed in § 2.

4.1. *Pattern of Variability: Continuum Bands*

Figure 4 shows the SWP and LWP continuum light curves as a function of Julian Date. The light curves show significant variations on a number of different timescales, particularly at short wavelengths. The variations are as large as 40%–50% on a timescale of several days and ~10% on a timescale of several hours. During the 9.3 days of continuous monitoring, there were four large-amplitude "events" of duration 2–3 days (minimum to minimum). These events are temporally well resolved, and they are easily recognized in each continuum wave band. Many of the shorter timescale, small-amplitude features also repeat in at least two different wave bands. The variations prior to and after the continuous-monitoring period are clearly undersampled and are of limited use, although it is evident that there were strong variations during the last 5 days of the monitoring period. It is clear from inspection of Figure 4 that the continuum variations are all highly correlated, with no discernable lag between the light curves. Paper IV shows that the continuum variations in different UV bands are all simultaneous to within ± 0.15 days.

Table 4 lists some basic properties of the variability in each wave band. The mean fluxes for the entire data set are given, as well as the mean errors, which are the average values of flux error divided by mean flux. F_{var}, the fractional variability, is the standard deviation of the fluxes divided by the mean flux in each wave band. It has been corrected to reflect the intrinsic variability by subtracting the mean error in quadrature. R_{max} is the ratio of largest to smallest mean flux in each wave band. It is clear from the parameters in Table 4 and from inspection of the light curves that there were significant variations in all continuum wave bands over this relatively short period of time. In particular, F_{var} is 4–10 times larger than the mean error, which is only ~1%–1.5%.

The amplitude of the continuum variations decreases with increasing wavelength, as was the case for NGC 5548 (Clavel et al. 1991) and NGC 3783 (Reichert et al. 1994). This can be seen in both the F_{var} and R_{max} parameters. This result is in general agreement with previous *IUE* studies of NGC 4151 (e.g., Perola et al. 1982), which found that for larger amplitude (but undersampled) variations, the UV continuum radiation hardens as it brightens. The combination of the well-sampled UV variations described in this paper with those in the optical (Paper II) and X-ray (Paper III) regions permits a more detailed examination of the behavior of continuum amplitude as a function of wavelength (see Paper IV).

4.2. *Pattern of Variability: Emission Lines*

Figure 5 shows the light curves for the strongest lines in the SWP region (as well as the continuum light curve at 1275 Å for comparison). The emission-line light curves are similar in appearance, with the fluxes rising through the first half of the campaign (over 8–9 days) and leveling off thereafter. C IV, the line with the smallest percentage errors, show evidence of a subsequent shallow dip of duration ~3 days in its light curve before recovering to the previous maximum. The He II and C III] light curves appear to reflect these trends, although they are noisier. There are also more rapid variations in the emission lines, particularly in the case of He II, which shows 15%–20% variations over a timescale of ~1 day. We cannot identify any source of systematic error that might produce these variations and, therefore, assume that they are real.

The light curves of the emission lines are substantially different in character from the continuum light curves. The large-amplitude continuum variations are very well defined and much more rapid than the emission-line variations. Presumably, the difference in the light curves is the result of a substantial response time of the lines to changes in the continuum, which will be explored in § 4.3.

Some basic properties of the emission-line variations are listed in Table 4. The fractional variability F_{var}, again corrected to reflect the intrinsic variability, and the ratio of largest to smallest flux, R_{max}, show that there were significant variations for all three emission lines. There is no obvious trend of larger variability amplitude for higher ionization lines, as was the case for NGC 5548 (Clavel et al. 1991) and NGC 3783 (Reichert et al. 1994), although we are restricted to only a few lines as a result of the small amplitude of variations over a short period of time and the complicated nature of the spectrum of NGC 4151. In light of previous studies, the larger amplitude of the He II variations is expected, but it is somewhat surprising that the amplitude of the C III] variations is larger than that of C IV.

4.3. *Time-Series Analysis*

Cross-correlation of a continuum light curve with a light curve from another continuum band or an emission-line light curve has been used in the past to determine whether the variations are correlated and if there is a time lag between the two series. Cross-correlations between the UV continuum light curves are given in Paper IV, to facilitate comparisons with other wavelength regions. For this paper, the continuum light curve at 1275 Å was cross-correlated with that of each emission-line feature, and in addition, the C IV light curve was cross-correlated with itself to generate its autocorrelation function (ACF). Two distinct correlation

TABLE 2

SWP FLUXES[a]

Image	Julian Date (2,440,000+)	F_λ(1275 Å)	F_λ(1440 Å)	F_λ(1820 Å)	F(C IV)	F(He II)	F(C III])
SWP 49333	9318.83535	36.94±0.34	33.77±0.51	25.67±0.34	38.49±0.68	4.48±0.18	5.38±0.11
SWP 49334	9318.88138	35.88±0.37	32.69±0.54	25.74±0.36	39.19±0.60	4.90±0.22	5.29±0.13
SWP 49335	9318.92616	36.63±0.36	32.25±0.52	25.01±0.35	39.62±0.58	5.00±0.24	5.30±0.15
SWP 49341	9319.81420	36.27±0.35	33.17±0.52	26.05±0.36	39.83±0.54	4.68±0.33	5.67±0.18
SWP 49342	9319.85965	38.64±0.37	34.15±0.53	26.84±0.36	39.37±0.63	4.50±0.37	5.72±0.24
SWP 49343	9319.90690	38.45±0.36	34.43±0.51	26.42±0.33	39.26±0.61	4.70±0.35	5.58±0.25
SWP 49362	9320.84159	37.98±0.37	34.53±0.53	27.91±0.35	38.76±0.55	5.29±0.23	5.57±0.20
SWP 49363	9320.88766	38.74±0.37	36.22±0.54	27.30±0.35	39.16±0.54	5.84±0.19	5.81±0.22
SWP 49364	9320.93306	38.50±0.36	35.37±0.53	27.29±0.36	39.49±0.68	5.69±0.18	5.95±0.20
SWP 49372	9321.83269	37.33±0.36	33.52±0.52	27.03±0.36	39.92±0.73	5.37±0.19	5.70±0.22
SWP 49373	9321.88064	38.89±0.36	34.12±0.51	27.00±0.34	40.72±0.73	5.24±0.19	5.54±0.19
SWP 49374	9321.92558	38.96±0.36	35.14±0.52	28.04±0.36	41.32±0.84	5.50±0.20	5.50±0.25
SWP 49379	9322.65037	40.47±0.37	36.60±0.54	27.52±0.35	42.46±0.89	5.53±0.21	5.58±0.28
SWP 49380	9322.70188	40.82±0.38	35.48±0.54	27.12±0.35	42.60±0.84	5.61±0.21	5.62±0.31
SWP 49381	9322.74602	39.94±0.38	36.52±0.54	28.53±0.37	42.00±0.65	5.89±0.21	5.78±0.23
SWP 49382	9322.79447	40.78±0.38	37.10±0.54	29.16±0.36	42.41±0.57	6.15±0.21	5.82±0.28
SWP 49383	9322.83888	43.33±0.39	37.15±0.54	28.81±0.35	42.79±0.62	6.26±0.24	5.56±0.21
SWP 49384	9322.91469	44.40±0.40	37.95±0.56	29.30±0.37	43.16±0.49	6.06±0.35	5.39±0.21
SWP 49385	9322.96032	44.46±0.40	38.17±0.55	28.89±0.37	42.97±0.60	6.15±0.58	5.51±0.21
SWP 49386	9323.01425	44.62±0.40	37.26±0.54	28.65±0.37	42.79±0.53	6.21±0.57	5.88±0.36
SWP 49387	9323.06480	44.77±0.40	38.53±0.55	29.28±0.37	43.26±0.60	6.30±0.47	6.01±0.40
SWP 49388	9323.11355	44.19±0.40	37.95±0.54	28.96±0.37	42.59±0.63	6.20±0.22	5.70±0.32
SWP 49389	9323.16836	44.75±0.40	38.15±0.55	30.17±0.36	42.11±0.74	6.06±0.21	5.92±0.20
SWP 49390	9323.24789	42.06±0.38	38.80±0.55	28.29±0.36	41.41±0.68	5.95±0.22	5.95±0.20
SWP 49391	9323.29455	42.95±0.38	39.81±0.55	29.06±0.35	41.97±0.69	5.93±0.31	6.02±0.20
SWP 49392	9323.34425	44.26±0.39	37.46±0.54	29.02±0.35	42.25±0.86	6.18±0.60	5.62±0.17
SWP 49393	9323.38736	43.13±0.39	37.70±0.55	29.19±0.36	43.03±1.02	6.37±0.58	5.68±0.14
SWP 49395	9323.57773	42.90±0.39	37.13±0.55	28.82±0.35	43.06±0.90	6.48±0.54	5.62±0.10
SWP 49396	9323.62746	42.76±0.39	36.19±0.53	29.21±0.35	43.59±0.72	6.21±0.23	5.72±0.09
SWP 49397	9323.67795	45.04±0.39	37.76±0.55	29.03±0.36	43.87±0.60	5.71±0.20	5.78±0.10
SWP 49398	9323.72733	43.03±0.39	37.63±0.55	29.49±0.37	43.80±0.64	5.46±0.20	5.78±0.12
SWP 49399	9323.77715	44.87±0.40	38.05±0.54	30.72±0.36	44.08±0.59	5.73±0.20	5.96±0.16
SWP 49400	9323.82148	44.56±0.39	38.83±0.55	29.58±0.36	44.74±0.62	6.02±0.22	5.67±0.22
SWP 49401	9323.89205	43.17±0.38	36.52±0.54	29.14±0.35	44.94±0.84	6.40±0.20	5.56±0.21
SWP 49402	9323.93686	42.46±0.39	37.87±0.55	29.62±0.36	44.38±0.83	6.56±0.19	5.48±0.19
SWP 49403	9323.98333	42.72±0.39	38.53±0.56	28.99±0.37	43.36±0.86	6.28±0.19	5.82±0.14
SWP 49404	9324.03740	42.48±0.39	37.01±0.54	28.95±0.37	43.56±0.60	6.34±0.26	6.27±0.15
SWP 49405	9324.08808	43.58±0.40	37.51±0.54	29.28±0.37	44.11±0.66	6.06±0.28	6.27±0.17
SWP 49406	9324.14307	44.02±0.40	36.08±0.54	27.86±0.37	43.98±0.64	6.58±0.28	5.93±0.15
SWP 49407	9324.19147	42.49±0.40	36.71±0.55	28.64±0.38	43.62±0.64	6.49±0.22	5.88±0.14
SWP 49408	9324.25170	43.40±0.39	37.95±0.54	28.67±0.35	42.58±0.53	6.83±0.18	5.62±0.14
SWP 49409	9324.29414	43.87±0.40	37.74±0.54	28.98±0.36	43.00±0.53	6.71±0.19	5.86±0.15
SWP 49410	9324.33682	42.18±0.39	37.40±0.54	27.94±0.37	43.25±0.48	6.56±0.19	6.01±0.24
SWP 49411	9324.38025	40.80±0.38	38.20±0.55	28.60±0.37	43.68±0.57	6.45±0.24	6.18±0.20
SWP 49412	9324.42285	40.96±0.38	36.84±0.54	28.82±0.36	43.60±0.68	6.10±0.30	6.02±0.20
SWP 49413	9324.56161	40.54±0.38	37.55±0.53	28.47±0.35	43.50±0.65	5.77±0.29	5.88±0.13
SWP 49414	9324.60663	40.99±0.38	36.94±0.53	28.32±0.36	42.83±0.78	5.86±0.28	5.88±0.14
SWP 49415	9324.65139	42.83±0.39	38.18±0.55	27.92±0.36	43.48±0.74	6.15±0.24	5.93±0.13
SWP 49416	9324.69515	40.93±0.39	36.25±0.56	27.91±0.37	43.86±0.75	6.56±0.27	5.77±0.18
SWP 49417	9324.73948	40.84±0.39	36.54±0.55	28.00±0.38	44.93±0.60	6.50±0.24	5.82±0.28
SWP 49418	9324.78458	40.18±0.38	35.57±0.53	28.06±0.35	43.57±0.56	6.38±0.23	5.91±0.29
SWP 49419	9324.83903	40.05±0.37	37.25±0.54	28.23±0.35	43.92±0.60	6.34±0.33	6.14±0.27
SWP 49420	9324.89620	38.89±0.37	35.22±0.53	28.41±0.35	44.32±0.68	6.20±0.34	6.37±0.21
SWP 49421	9324.94267	40.48±0.38	34.97±0.53	27.98±0.35	44.72±0.69	6.51±0.36	6.77±0.20
SWP 49422	9324.98905	39.73±0.38	35.68±0.53	27.22±0.35	44.38±0.71	6.11±0.25	6.53±0.16
SWP 49423	9325.04013	38.47±0.36	34.92±0.53	27.95±0.37	44.06±0.65	5.69±0.25	6.05±0.21
SWP 49424	9325.08877	38.85±0.37	35.57±0.54	27.35±0.35	44.30±0.67	5.98±0.24	5.37±0.21
SWP 49425	9325.13619	39.25±0.37	35.18±0.53	27.93±0.36	44.11±0.65	6.47±0.24	6.01±0.26
SWP 49426	9325.18171	40.78±0.39	35.55±0.54	27.22±0.36	43.72±0.64	6.53±0.23	6.26±0.22
SWP 49427	9325.24969	38.40±0.38	36.69±0.55	28.28±0.37	44.11±0.52	6.28±0.22	6.77±0.23
SWP 49429	9325.35080	39.54±0.36	36.11±0.51	28.09±0.35	44.02±0.43	5.99±0.21	6.29±0.22
SWP 49430	9325.40051	40.56±0.37	37.03±0.54	28.54±0.37	44.78±0.38	6.10±0.26	6.30±0.21
SWP 49431	9325.54334	40.26±0.38	38.19±0.54	29.18±0.36	44.76±0.45	6.10±0.27	6.23±0.21
SWP 49432	9325.58506	43.89±0.39	39.03±0.55	29.38±0.37	45.18±0.56	6.59±0.33	6.40±0.26
SWP 49433	9325.62936	44.22±0.40	39.37±0.56	29.18±0.37	46.05±0.69	7.09±0.28	6.42±0.25
SWP 49434	9325.67491	44.49±0.47	39.89±0.69	29.14±0.47	45.77±0.79	7.35±0.29	6.34±0.33
SWP 49435	9325.71769	46.26±0.51	39.38±0.72	30.02±0.51	45.84±0.81	7.22±0.24	6.24±0.26

TABLE 2—*Continued*

Image	Julian Date (2,440,000+)	F_λ(1275 Å)	F_λ(1440 Å)	F_λ(1820 Å)	F(C IV)	F(He II)	F(C III])
SWP 49436	9325.76265	46.18±0.44	39.56±0.60	29.99±0.42	44.19±0.78	7.36±0.24	6.28±0.32
SWP 49437	9325.80630	45.30±0.44	40.89±0.61	29.07±0.40	44.93±0.79	7.13±0.20	6.21±0.25
SWP 49438	9325.87929	43.74±0.42	38.75±0.58	30.03±0.38	44.55±0.77	7.22±0.19	6.22±0.24
SWP 49439	9325.92424	45.82±0.42	38.96±0.58	30.02±0.39	44.85±0.77	6.87±0.20	6.20±0.17
SWP 49440	9325.96878	46.67±0.42	39.78±0.59	30.29±0.39	44.81±0.67	6.80±0.26	6.47±0.14
SWP 49441	9326.01227	45.57±0.42	39.34±0.59	30.09±0.40	45.72±0.57	6.38±0.28	6.85±0.22
SWP 49442	9326.05646	47.47±0.43	38.45±0.59	29.17±0.40	45.87±0.55	6.28±0.31	6.97±0.25
SWP 49443	9326.10977	46.90±0.43	40.38±0.60	30.65±0.40	45.21±0.57	6.10±0.46	7.00±0.31
SWP 49444	9326.15278	48.47±0.45	42.31±0.62	30.24±0.40	45.24±0.57	6.57±0.47	6.55±0.27
SWP 49445	9326.19659	49.80±0.45	41.71±0.61	32.03±0.42	46.45±0.57	6.52±0.46	6.66±0.27
SWP 49446	9326.25544	50.09±0.44	42.74±0.60	32.27±0.41	46.95±0.63	6.72±0.24	6.75±0.24
SWP 49447	9326.29883	50.15±0.43	43.76±0.59	32.46±0.39	46.25±0.74	6.79±0.20	7.11±0.20
SWP 49448	9326.34414	49.78±0.44	42.86±0.61	31.66±0.41	45.11±0.76	7.19±0.19	7.05±0.21
SWP 49449	9326.38745	51.45±0.46	43.07±0.63	32.51±0.41	45.78±0.70	7.13±0.30	7.12±0.20
SWP 49450	9326.54594	51.54±0.45	41.72±0.60	32.27±0.40	45.58±0.72	7.21±0.29	6.90±0.20
SWP 49451	9326.58498	51.92±0.43	43.35±0.57	31.62±0.38	46.94±0.78	7.40±0.51	7.04±0.28
SWP 49452	9326.62965	51.47±0.48	44.34±0.65	32.71±0.45	46.47±0.82	7.55±0.47	7.20±0.28
SWP 49453	9326.67189	52.30±0.52	44.99±0.73	32.64±0.51	47.71±0.89	7.20±0.49	7.88±0.35
SWP 49454	9326.71376	53.92±0.58	44.25±0.80	32.78±0.57	47.38±0.92	7.00±0.33	7.82±0.23
SWP 49455	9326.75653	54.34±0.50	44.79±0.68	32.78±0.46	47.79±0.85	7.11±0.28	7.71±0.24
SWP 49456	9326.80056	52.24±0.44	43.07±0.57	31.38±0.39	47.14±0.73	7.27±0.41	7.22±0.27
SWP 49457	9326.85309	52.83±0.44	43.80±0.57	31.92±0.37	46.76±0.67	7.16±0.34	7.15±0.27
SWP 49458	9326.92141	52.52±0.46	43.02±0.62	30.89±0.39	46.19±0.66	7.03±0.35	7.24±0.31
SWP 49459	9326.97450	51.37±0.45	44.24±0.62	31.01±0.41	46.87±0.70	6.72±0.26	7.16±0.22
SWP 49460	9327.02091	51.17±0.44	42.85±0.61	31.63±0.39	46.78±0.62	6.64±0.20	7.06±0.26
SWP 49461	9327.06616	51.00±0.44	43.26±0.61	31.33±0.38	47.69±0.58	6.68±0.20	6.90±0.20
SWP 49462	9327.11621	51.17±0.45	43.05±0.61	30.88±0.41	47.93±0.56	7.01±0.21	7.14±0.28
SWP 49463	9327.16354	49.42±0.44	41.89±0.61	30.63±0.39	47.49±0.61	7.15±0.26	7.32±0.28
SWP 49464	9327.22521	51.86±0.46	44.27±0.62	31.99±0.42	47.53±0.72	7.38±0.27	7.16±0.26
SWP 49465	9327.26920	51.15±0.48	40.48±0.63	31.94±0.42	47.08±0.79	7.32±0.24	6.86±0.24
SWP 49466	9327.32016	49.79±0.46	41.82±0.63	31.77±0.42	48.08±0.99	7.61±0.22	6.75±0.26
SWP 49467	9327.37336	49.57±0.47	40.09±0.63	30.33±0.42	47.97±0.85	7.26±0.24	6.79±0.34
SWP 49468	9327.41718	48.81±0.44	40.46±0.62	30.55±0.40	47.09±0.85	7.23±0.32	6.84±0.35
SWP 49470	9327.53474	47.47±0.44	39.41±0.62	29.22±0.40	46.57±0.67	6.68±0.34	6.94±0.32
SWP 49471	9327.57271	47.10±0.44	39.23±0.60	29.87±0.40	46.72±0.78	6.70±0.31	6.70±0.23
SWP 49472	9327.61983	47.01±0.46	39.15±0.63	30.42±0.44	46.96±0.89	6.55±0.28	6.74±0.21
SWP 49473	9327.66413	47.94±0.50	41.75±0.73	29.56±0.51	48.11±0.89	7.04±0.29	7.03±0.24
SWP 49474	9327.70602	48.37±0.55	40.86±0.79	29.61±0.55	48.80±0.87	6.88±0.30	7.15±0.27
SWP 49475	9327.75097	47.19±0.47	40.05±0.65	30.05±0.46	49.19±0.66	7.29±0.26	7.24±0.20
SWP 49476	9327.79381	45.03±0.40	38.57±0.55	30.33±0.37	48.26±0.52	6.94±0.21	6.95±0.18
SWP 49477	9327.84021	43.71±0.39	39.64±0.55	29.18±0.36	47.38±0.52	7.25±0.21	6.72±0.22
SWP 49478	9327.89870	43.53±0.39	36.42±0.54	28.92±0.39	48.02±0.54	7.00±0.18	6.70±0.20
SWP 49479	9327.94343	44.60±0.40	35.76±0.53	29.03±0.37	48.83±0.57	6.80±0.18	6.59±0.23
SWP 49480	9327.99028	44.04±0.39	36.03±0.53	29.09±0.36	49.18±0.55	6.70±0.19	6.94±0.24
SWP 49481	9328.03307	43.47±0.39	36.94±0.54	28.37±0.36	48.56±0.54	6.64±0.22	6.67±0.25
SWP 49482	9328.08648	43.17±0.38	37.14±0.55	28.97±0.37	48.82±0.57	6.97±0.26	6.63±0.26
SWP 49483	9328.12875	43.58±0.39	36.71±0.54	28.49±0.36	48.61±0.67	7.10±0.28	6.61±0.21
SWP 49484	9328.17417	44.02±0.41	37.57±0.56	29.56±0.38	48.55±0.59	7.22±0.29	6.50±0.25
SWP 49485	9328.22543	44.13±0.40	39.36±0.57	29.17±0.37	47.93±0.58	6.84±0.27	6.78±0.32
SWP 49486	9328.27341	45.21±0.41	37.89±0.55	28.36±0.37	48.30±0.48	6.98±0.22	6.69±0.36
SWP 49487	9328.31764	44.23±0.42	36.73±0.58	29.20±0.39	48.96±0.57	6.84±0.22	6.79±0.30
SWP 49488	9328.36374	43.37±0.41	36.78±0.57	28.65±0.39	49.16±0.61	7.12±0.21	6.42±0.16
SWP 49489	9328.40705	42.54±0.41	36.43±0.57	28.37±0.39	47.95±0.59	6.75±0.23	6.23±0.12
SWP 49491	9328.54118	41.44±0.39	36.09±0.55	28.39±0.36	47.40±0.60	6.57±0.43	6.25±0.13
SWP 49492	9328.58108	42.24±0.38	37.51±0.53	29.15±0.35	46.86±0.73	6.67±0.46	6.19±0.13
SWP 49493	9328.62321	44.05±0.40	39.17±0.56	28.60±0.37	46.39±0.75	6.21±0.45	6.54±0.13
SWP 49494	9328.66607	44.99±0.45	40.74±0.64	26.70±0.42	46.52±0.90	6.23±0.51	6.79±0.15
SWP 49495	9328.70771	44.55±0.49	39.58±0.70	28.54±0.47	47.16±0.84	5.72±0.49	7.28±0.23
SWP 49496	9328.75026	45.09±0.43	39.34±0.61	28.59±0.41	47.94±0.81	6.34±0.48	7.19±0.30
SWP 49497	9328.79306	44.29±0.38	39.06±0.52	28.89±0.35	47.51±0.62	6.65±0.22	6.94±0.35
SWP 49498	9328.84015	44.15±0.37	38.77±0.52	29.33±0.34	47.01±0.54	6.84±0.22	6.72±0.28
SWP 49499	9328.89331	45.56±0.40	38.92±0.55	29.35±0.36	48.30±0.62	6.69±0.43	6.61±0.27
SWP 49500	9328.93673	44.60±0.40	38.40±0.56	29.54±0.38	48.85±0.67	6.55±0.42	6.62±0.21
SWP 49501	9328.98288	46.95±0.41	37.86±0.55	29.53±0.37	48.88±0.65	7.03±0.41	6.84±0.24
SWP 49502	9329.02826	46.42±0.41	39.13±0.55	30.19±0.38	48.53±0.53	7.30±0.20	7.00±0.20
SWP 49503	9329.07162	46.76±0.41	40.09±0.56	29.47±0.38	48.05±0.51	7.28±0.19	6.83±0.20
SWP 49504	9329.11318	48.05±0.42	40.57±0.57	31.07±0.38	48.17±0.62	6.94±0.22	6.43±0.18
SWP 49505	9329.15711	48.60±0.42	39.76±0.56	30.79±0.37	47.55±0.71	6.99±0.22	6.23±0.19
SWP 49506	9329.21402	48.63±0.42	39.20±0.55	30.49±0.37	48.04±0.69	7.29±0.23	6.53±0.17

TABLE 2—*Continued*

Image	Julian Date (2,440,000+)	F_λ(1275 Å)	F_λ(1440 Å)	F_λ(1820 Å)	F(C IV)	F(He II)	F(C III])
SWP 49507	9329.25431	46.39±0.41	40.41±0.58	29.67±0.37	48.02±0.57	7.57±0.20	6.71±0.27
SWP 49508	9329.30167	47.39±0.42	39.23±0.57	31.00±0.38	48.53±0.64	7.23±0.22	6.86±0.28
SWP 49509	9329.34620	48.32±0.43	38.12±0.57	30.42±0.39	47.28±0.64	6.96±0.22	6.59±0.28
SWP 49510	9329.39206	46.53±0.40	38.39±0.54	30.24±0.36	46.92±0.68	6.61±0.22	6.66±0.18
SWP 49511	9329.43838	45.96±0.38	37.24±0.52	29.37±0.38	45.84±0.61	7.08±0.19	6.64±0.16
SWP 49512	9329.53191	43.49±0.40	37.42±0.54	28.62±0.35	47.12±0.65	7.21±0.20	6.83±0.19
SWP 49513	9329.57171	42.53±0.40	38.08±0.56	28.90±0.38	47.38±0.79	7.42±0.25	6.81±0.31
SWP 49514	9329.61359	41.83±0.39	36.20±0.55	28.13±0.37	47.73±0.90	6.98±0.27	7.15±0.31
SWP 49515	9329.65601	42.03±0.38	36.54±0.53	27.52±0.35	47.13±0.83	6.56±0.27	7.09±0.30
SWP 49516	9329.69817	41.61±0.40	37.08±0.57	28.47±0.39	46.92±0.70	6.57±0.21	6.98±0.22
SWP 49517	9329.74183	41.36±0.39	35.82±0.56	28.15±0.36	47.67±0.62	6.66±0.22	6.88±0.23
SWP 49518	9329.78385	41.00±0.39	35.42±0.55	27.98±0.37	48.27±0.63	6.77±0.24	6.98±0.32
SWP 49519	9329.83279	39.59±0.37	35.42±0.53	26.35±0.35	47.72±0.78	6.66±0.29	7.06±0.29
SWP 49520	9329.88559	39.88±0.38	35.86±0.53	27.86±0.35	46.54±0.74	6.58±0.30	6.75±0.28
SWP 49521	9329.92980	39.54±0.37	35.97±0.53	27.71±0.36	45.57±0.83	6.73±0.29	6.72±0.14
SWP 49522	9329.97655	40.39±0.37	35.03±0.53	26.92±0.36	46.29±0.71	6.71±0.26	6.65±0.25
SWP 49523	9330.02228	41.22±0.38	35.18±0.54	27.46±0.35	45.75±0.72	6.66±0.24	6.37±0.25
SWP 49524	9330.07459	39.21±0.38	35.99±0.53	27.65±0.35	46.72±0.62	6.49±0.22	6.19±0.26
SWP 49525	9330.11640	40.12±0.37	34.36±0.53	27.99±0.37	46.60±0.61	6.30±0.20	6.25±0.16
SWP 49526	9330.15976	39.59±0.38	35.34±0.53	28.89±0.36	47.27±0.61	6.47±0.19	6.64±0.17
SWP 49527	9330.21123	40.55±0.39	35.67±0.54	27.06±0.35	46.62±0.75	6.33±0.27	6.69±0.24
SWP 49528	9330.25175	39.23±0.37	37.48±0.55	28.43±0.36	46.49±0.66	6.46±0.30	6.56±0.22
SWP 49529	9330.29745	40.00±0.37	36.35±0.54	27.69±0.36	46.99±0.60	6.27±0.29	6.75±0.23
SWP 49530	9330.34584	41.40±0.39	36.12±0.53	27.55±0.35	47.12±0.50	6.25±0.24	6.92±0.14
SWP 49531	9330.38880	40.99±0.39	35.30±0.56	27.70±0.38	47.38±0.58	6.12±0.20	7.01±0.15
SWP 49533	9330.52881	40.17±0.37	36.27±0.54	27.31±0.36	47.68±0.52	5.90±0.19	6.77±0.12
SWP 49534	9330.56726	40.60±0.39	36.10±0.55	27.63±0.36	47.17±0.55	6.15±0.27	6.55±0.15
SWP 49535	9330.61240	40.62±0.39	36.28±0.54	28.20±0.36	46.99±0.48	6.25±0.29	6.59±0.15
SWP 49536	9330.65634	41.61±0.40	36.11±0.57	27.25±0.39	47.06±0.59	6.42±0.34	6.28±0.16
SWP 49537	9330.70314	42.72±0.42	35.75±0.57	28.00±0.39	48.06±0.47	6.65±0.26	6.45±0.13
SWP 49538	9330.74627	41.34±0.40	35.37±0.56	28.47±0.38	48.06±0.69	6.71±0.30	6.69±0.15
SWP 49539	9330.79020	41.48±0.38	36.60±0.54	27.40±0.35	47.59±0.60	6.58±0.29	7.14±0.27
SWP 49540	9330.84397	43.04±0.40	36.15±0.54	27.59±0.36	47.97±0.66	6.42±0.30	7.15±0.27
SWP 49541	9330.90933	42.04±0.39	36.29±0.54	28.65±0.37	46.96±0.60	6.59±0.29	6.72±0.24
SWP 49542	9330.96370	43.17±0.39	37.70±0.55	28.87±0.35	47.06±0.82	6.52±0.29	6.84±0.12
SWP 49543	9331.00844	43.52±0.40	36.20±0.54	27.81±0.36	47.00±0.83	6.32±0.28	6.88±0.16
SWP 49544	9331.05978	43.31±0.39	35.28±0.53	28.02±0.37	48.14±0.74	6.50±0.26	7.16±0.22
SWP 49545	9331.10807	43.32±0.40	36.43±0.54	28.72±0.37	47.65±0.53	6.75±0.25	6.77±0.25
SWP 49546	9331.15458	43.62±0.40	36.61±0.54	27.57±0.35	45.67±0.57	6.59±0.23	6.66±0.30
SWP 49547	9331.21365	43.33±0.39	39.14±0.53	28.89±0.36	46.42±0.52	6.17±0.20	6.64±0.22
SWP 49548	9331.25499	42.40±0.38	36.51±0.53	28.49±0.36	47.47±0.70	6.22±0.18	7.05±0.23
SWP 49549	9331.30012	42.43±0.39	37.21±0.53	28.07±0.36	49.74±0.77	6.62±0.29	6.85±0.16
SWP 49550	9331.34586	42.94±0.38	35.37±0.52	28.85±0.38	49.38±0.85	6.57±0.29	6.80±0.18
SWP 49551	9331.38575	42.06±0.38	36.13±0.54	27.58±0.34	47.93±0.72	6.91±0.28	6.39±0.23
SWP 49553	9331.51858	39.24±0.38	35.27±0.54	26.32±0.36	47.15±0.53	7.02±0.17	6.45±0.22
SWP 49554	9331.55876	38.16±0.36	35.14±0.54	27.21±0.36	46.50±0.58	7.32±0.17	6.51±0.29
SWP 49555	9331.60369	40.15±0.38	35.14±0.53	27.78±0.36	47.06±0.66	6.99±0.33	6.92±0.28
SWP 49556	9331.64840	39.85±0.40	36.62±0.57	27.02±0.37	47.80±0.94	7.10±0.36	7.34±0.29
SWP 49557	9331.69266	39.22±0.40	35.56±0.59	27.18±0.41	47.84±0.99	7.03±0.37	7.59±0.24
SWP 49558	9331.73834	37.72±0.39	33.90±0.55	26.24±0.38	48.53±0.92	6.91±0.25	7.37±0.19
SWP 49559	9331.80425	36.86±0.39	32.47±0.55	26.44±0.36	48.13±0.71	6.31±0.23	7.05±0.18
SWP 49560	9331.85256	37.09±0.37	30.99±0.53	25.94±0.36	48.12±0.71	6.19±0.27	6.61±0.18
SWP 49567	9332.75464	42.61±0.38	36.73±0.55	27.48±0.35	48.88±0.67	6.51±0.24	6.57±0.25
SWP 49568	9332.80381	41.76±0.38	36.39±0.54	29.26±0.36	48.60±0.62	7.07±0.23	6.88±0.30
SWP 49569	9332.85104	42.67±0.39	36.40±0.54	28.21±0.35	48.66±0.48	7.16±0.18	6.74±0.31
SWP 49574	9333.74031	38.47±0.36	33.57±0.52	27.45±0.37	47.80±0.49	7.07±0.21	6.71±0.26
SWP 49575	9333.78330	38.26±0.33	34.03±0.47	26.67±0.31	48.21±0.61	6.94±0.20	6.55±0.24
SWP 49576	9333.82860	38.13±0.32	33.49±0.45	26.55±0.30	49.15±0.60	6.85±0.20	6.75±0.22
SWP 49582	9334.75142	37.84±0.34	32.84±0.46	26.27±0.31	49.13±0.58	6.71±0.20	6.66±0.18
SWP 49583	9334.79190	37.45±0.35	32.91±0.49	26.46±0.32	48.26±0.71	6.47±0.50	6.53±0.17
SWP 49584	9334.83455	38.30±0.35	35.54±0.49	26.37±0.31	47.20±0.73	6.55±0.50	6.81±0.17
SWP 49592	9335.74617	42.78±0.36	36.36±0.49	27.49±0.33	46.59±0.82	6.52±0.52	6.87±0.15
SWP 49593	9335.78609	42.27±0.36	36.11±0.49	28.79±0.34	47.50±0.66	6.46±0.22	7.00±0.15
SWP 49594	9335.83018	41.66±0.36	36.89±0.49	27.81±0.33	48.59±0.68	6.60±0.22	6.62±0.14
SWP 49600	9336.75053	44.35±0.37	37.02±0.50	29.86±0.34	49.99±0.58	6.78±0.21	6.51±0.15
SWP 49601	9336.79082	42.41±0.35	35.61±0.48	28.08±0.32	50.55±0.53	7.16±0.19	6.56±0.16
SWP 49602	9336.82708	44.31±0.37	36.54±0.50	28.63±0.33	51.06±0.48	7.22±0.14	7.11±0.22

[a] Rest-frame continuum fluxes in units of 10^{-14} ergs s^{-1} cm^{-2} Å^{-1}; rest-frame line fluxes in units of 10^{-12} ergs s^{-1} cm^{-2}.

TABLE 3

LWP FLUXES[a]

Image	Julian Date (2,440,000+)	F_λ(2688 Å)	Image	Julian Date (2,440,000+)	F_λ(2688 Å)
LWP 26815	9318.85602	17.92±0.20	LWP 26893	9325.23022	19.15±0.20
LWP 26816	9318.90362	17.75±0.18	LWP 26896	9325.37193	19.27±0.22
LWP 26817	9318.94549	17.92±0.18	LWP 26897	9325.42154	19.44±0.22
LWP 26822	9319.83692	17.83±0.18	LWP 26898	9325.55997	19.00±0.22
LWP 26823	9319.87985	17.82±0.19	LWP 26899	9325.60505	19.20±0.22
LWP 26824	9319.92803	17.41±0.19	LWP 26900	9325.65110	19.74±0.24
LWP 26831	9320.86331	18.00±0.19	LWP 26901	9325.69425	20.04±0.28
LWP 26832	9320.91007	18.12±0.17	LWP 26902	9325.73752	20.67±0.27
LWP 26836	9321.85620	18.00±0.18	LWP 26903	9325.78252	19.54±0.23
LWP 26837	9321.90200	18.39±0.18	LWP 26904	9325.83486	18.98±0.23
LWP 26838	9321.94529	18.17±0.19	LWP 26905	9325.89709	19.79±0.23
LWP 26846	9322.67571	18.48±0.20	LWP 26906	9325.94435	19.88±0.23
LWP 26847	9322.72296	18.77±0.20	LWP 26907	9325.98786	19.92±0.23
LWP 26848	9322.76984	18.76±0.20	LWP 26908	9326.03159	20.25±0.23
LWP 26849	9322.81449	18.84±0.20	LWP 26909	9326.08428	19.72±0.24
LWP 26850	9322.88833	19.36±0.20	LWP 26910	9326.12891	19.86±0.24
LWP 26851	9322.93730	19.15±0.20	LWP 26911	9326.17253	20.16±0.24
LWP 26852	9322.98483	19.17±0.20	LWP 26912	9326.23507	20.59±0.23
LWP 26853	9323.03668	19.29±0.20	LWP 26913	9326.27462	20.25±0.23
LWP 26854	9323.08673	19.09±0.20	LWP 26914	9326.32039	20.51±0.24
LWP 26855	9323.13972	19.27±0.20	LWP 26915	9326.36429	20.43±0.25
LWP 26856	9323.22432	19.86±0.20	LWP 26916	9326.40734	20.76±0.24
LWP 26857	9323.26862	19.31±0.22	LWP 26917	9326.56074	20.82±0.24
LWP 26858	9323.31392	19.39±0.22	LWP 26918	9326.60631	20.66±0.25
LWP 26859	9323.36330	19.46±0.22	LWP 26919	9326.64889	20.82±0.26
LWP 26860	9323.40693	19.40±0.22	LWP 26920	9326.69127	21.29±0.30
LWP 26861	9323.55218	19.16±0.22	LWP 26921	9326.73370	20.86±0.30
LWP 26862	9323.59907	19.22±0.22	LWP 26922	9326.77600	21.01±0.25
LWP 26863	9323.64899	19.38±0.22	LWP 26923	9326.81910	20.64±0.24
LWP 26864	9323.69892	19.49±0.22	LWP 26924	9326.89598	21.07±0.24
LWP 26865	9323.74873	19.41±0.22	LWP 26925	9326.94789	20.74±0.23
LWP 26866	9323.79730	19.60±0.22	LWP 26926	9326.99395	20.83±0.24
LWP 26867	9323.84314	19.78±0.22	LWP 26927	9327.04029	20.95±0.24
LWP 26868	9323.91324	19.18±0.20	LWP 26928	9327.09056	21.08±0.24
LWP 26869	9323.95897	19.28±0.20	LWP 26929	9327.13751	20.84±0.24
LWP 26870	9324.00767	19.42±0.20	LWP 26930	9327.19061	21.04±0.25
LWP 26871	9324.05895	19.18±0.20	LWP 26932	9327.29420	20.97±0.24
LWP 26872	9324.11755	18.95±0.20	LWP 26933	9327.33920	21.20±0.24
LWP 26873	9324.16673	19.18±0.20	LWP 26934	9327.39288	20.78±0.25
LWP 26874	9324.23083	19.14±0.22	LWP 26935	9327.54927	20.56±0.24
LWP 26875	9324.27104	19.35±0.22	LWP 26936	9327.59721	20.56±0.24
LWP 26876	9324.31343	19.40±0.22	LWP 26937	9327.63990	20.95±0.26
LWP 26877	9324.35664	19.45±0.22	LWP 26938	9327.68222	21.57±0.33
LWP 26878	9324.39969	19.31±0.22	LWP 26939	9327.72759	21.12±0.29
LWP 26879	9324.54413	18.53±0.21	LWP 26940	9327.77062	20.38±0.23
LWP 26880	9324.58134	18.88±0.21	LWP 26941	9327.81279	20.38±0.22
LWP 26881	9324.62566	19.51±0.22	LWP 26942	9327.87748	20.40±0.22
LWP 26882	9324.67076	18.79±0.22	LWP 26943	9327.91932	20.83±0.22
LWP 26883	9324.71550	18.87±0.23	LWP 26944	9327.96603	20.37±0.22
LWP 26884	9324.76015	18.99±0.22	LWP 26945	9328.00942	20.35±0.22
LWP 26885	9324.80494	18.58±0.21	LWP 26946	9328.06204	20.54±0.22
LWP 26886	9324.87563	19.21±0.20	LWP 26947	9328.10593	20.60±0.22
LWP 26887	9324.91875	18.95±0.20	LWP 26948	9328.14762	20.28±0.23
LWP 26888	9324.96537	18.89±0.20	LWP 26949	9328.20417	20.33±0.23
LWP 26889	9325.00846	19.25±0.20	LWP 26950	9328.24645	20.45±0.23
LWP 26890	9325.06462	19.07±0.20	LWP 26951	9328.29373	20.66±0.23
LWP 26891	9325.10877	18.85±0.20	LWP 26952	9328.33689	20.66±0.24
LWP 26892	9325.15744	18.82±0.20	LWP 26953	9328.38307	20.18±0.23
LWP 26954	9328.55602	19.67±0.23	LWP 26992	9330.36723	20.14±0.22
LWP 26955	9328.59917	21.06±0.23	LWP 26993	9330.41095	19.83±0.22
LWP 26956	9328.64231	20.77±0.25	LWP 26994	9330.54402	19.61±0.22
LWP 26957	9328.68395	20.87±0.28	LWP 26995	9330.58879	19.44±0.22
LWP 26958	9328.72639	21.36±0.29	LWP 26996	9330.63270	20.07±0.22
LWP 26959	9328.76899	20.26±0.23	LWP 26997	9330.67968	20.87±0.24
LWP 26960	9328.81123	20.22±0.22	LWP 26998	9330.72290	21.63±0.25
LWP 26961	9328.87379	20.70±0.21	LWP 26999	9330.76601	21.46±0.24
LWP 26962	9328.91296	20.56±0.22	LWP 27000	9330.81270	20.24±0.23

TABLE 3—*Continued*

Image	Julian Date (2,440,000+)	F_λ(2688 Å)	Image	Julian Date (2,440,000+)	F_λ(2688 Å)
LWP 26963	9328.95503	20.49±0.22	LWP 27001	9330.88433	19.60±0.22
LWP 26964	9329.00142	20.84±0.23	LWP 27002	9330.93458	20.11±0.23
LWP 26965	9329.04812	21.26±0.23	LWP 27003	9330.98451	20.02±0.22
LWP 26966	9329.08977	20.84±0.23	LWP 27004	9331.02991	20.42±0.23
LWP 26967	9329.13165	21.19±0.23	LWP 27005	9331.08154	20.42±0.23
LWP 26968	9329.17823	20.97±0.23	LWP 27006	9331.13067	20.50±0.23
LWP 26969	9329.23031	20.88±0.24	LWP 27007	9331.17780	20.30±0.23
LWP 26970	9329.27590	20.92±0.24	LWP 27009	9331.27549	19.88±0.22
LWP 26971	9329.32187	21.00±0.24	LWP 27010	9331.32125	19.83±0.23
LWP 26972	9329.36632	20.68±0.24	LWP 27012	9331.40681	19.52±0.23
LWP 26973	9329.41200	20.13±0.23	LWP 27013	9331.53384	19.20±0.22
LWP 26974	9329.54823	20.50±0.22	LWP 27014	9331.58003	19.96±0.22
LWP 26975	9329.59112	20.43±0.22	LWP 27015	9331.62443	19.72±0.22
LWP 26976	9329.63353	20.07±0.22	LWP 27016	9331.66881	20.02±0.23
LWP 26977	9329.67546	19.43±0.22	LWP 27017	9331.71460	19.90±0.24
LWP 26978	9329.71931	19.46±0.22	LWP 27019	9331.82530	19.44±0.23
LWP 26979	9329.76061	19.53±0.22	LWP 27024	9332.78837	20.31±0.22
LWP 26980	9329.80323	19.43±0.22	LWP 27025	9332.82462	20.56±0.22
LWP 26981	9329.86347	19.19±0.22	LWP 27030	9333.75813	19.64±0.21
LWP 26982	9329.90594	18.75±0.21	LWP 27031	9333.80360	19.82±0.19
LWP 26983	9329.94869	19.03±0.21	LWP 27032	9333.84854	19.86±0.19
LWP 26984	9329.99855	18.73±0.21	LWP 27034	9334.76765	19.32±0.19
LWP 26985	9330.04741	19.24±0.22	LWP 27035	9334.81023	19.93±0.21
LWP 26986	9330.09278	18.88±0.21	LWP 27036	9334.85409	19.29±0.20
LWP 26987	9330.13465	19.05±0.22	LWP 27040	9335.76131	19.98±0.19
LWP 26988	9330.17782	19.12±0.22	LWP 27041	9335.80560	20.07±0.21
LWP 26989	9330.22801	19.56±0.22	LWP 27042	9335.84938	20.29±0.20
LWP 26990	9330.27389	19.53±0.22	LWP 27048	9336.76696	20.01±0.20
LWP 26991	9330.31899	19.72±0.22	LWP 27050	9336.85257	20.08±0.21

[a] Rest-frame continuum fluxes in units of 10^{-14} ergs s^{-1} cm^{-2} Å^{-1}.

TABLE 4

VARIABILITY PARAMETERS

Feature	Mean Flux[a]	Mean Error	F_{var}	R_{max}
F_λ(1275 Å).....	43.45	0.009	0.091	1.51
F_λ(1440 Å).....	37.66	0.015	0.070	1.45
F_λ(1820 Å).....	28.83	0.013	0.052	1.31
F_λ(2688 Å).....	19.83	0.011	0.042	1.24
F(C IV).....	45.95	0.014	0.054	1.33
F(He II)	6.54	0.042	0.077	1.70
F(C III]).....	6.50	0.034	0.077	1.49

[a] Continuum fluxes in units of 10^{-14} ergs s^{-1} cm^{-2} Å^{-1}; line fluxes in units of 10^{-12} ergs s^{-1} cm^{-2}.

functions were calculated: the interpolation cross-correlation function (CCF; see Gaskell & Sparke 1986; Gaskell & Peterson 1987) and the discrete correlation function (DCF; see Edelson & Krolik 1988). The correlations were calculated in the manner described by White & Peterson (1994). The calculations were performed for the subset of data obtained during the continuous-monitoring period and for all data obtained during the *IUE* campaign. The sampling interval chosen was 0.5 days (72 minutes), which is the approximate interval between consecutive observations with a particular camera during the continuous-monitoring period.

Figures 6 and 7 show the emission-line CCFs and DCFs for the continuous and entire data sets, respectively. The uniform sampling is responsible for the agreement between CCFs and DCFs in Figure 6. In Figure 7, after a long span of data is included, both CCF and DCF values are higher in the 1–5 day regime, and additional peaks in the correlation functions appear. The CCF and DCF values for the entire data set are similar but do not agree exactly, because the weighting is different; the DCF is based on the data points only, whereas the CCF relies on interpolated data as well (see Gaskell, Koratkar, & Sparke 1989).

Figure 6 indicates that the emission-line variations are not well correlated with the continuum variations; the peak values of the CCFs are only 0.42, 0.58, and 0.47 for C IV, He II, and C III], respectively. This is not a surprise, since the continuum and emission-light curves are so different. In addition, the CCFs and DCFs shown in Figure 7 for the entire data set exhibit multiple peaks. This is a result of the fact that the continuum light curves show several quick events during the monitoring period whereas the emission-line light curves show only one well-defined event of longer duration. The best case for a significant result comes from the He II correlations, which show a fairly well defined peak at a lag of $\sim$0.2 days. This *suggests* the presence of a component of He II emission that responds to continuum variations on very short timescales, although this component does not appear to be the major one.

The principal timescale for continuum changes in this campaign appears to be substantially shorter than the characteristic response times of the emission lines, as indicated by the small FWHM of the ACF for the 1275 Å continuum band (1.2 days; see Paper IV) compared to that for C IV (4.4 days; see Fig. 6). Since the continuum and emission-line light curves are so dissimilar, the correlation functions are

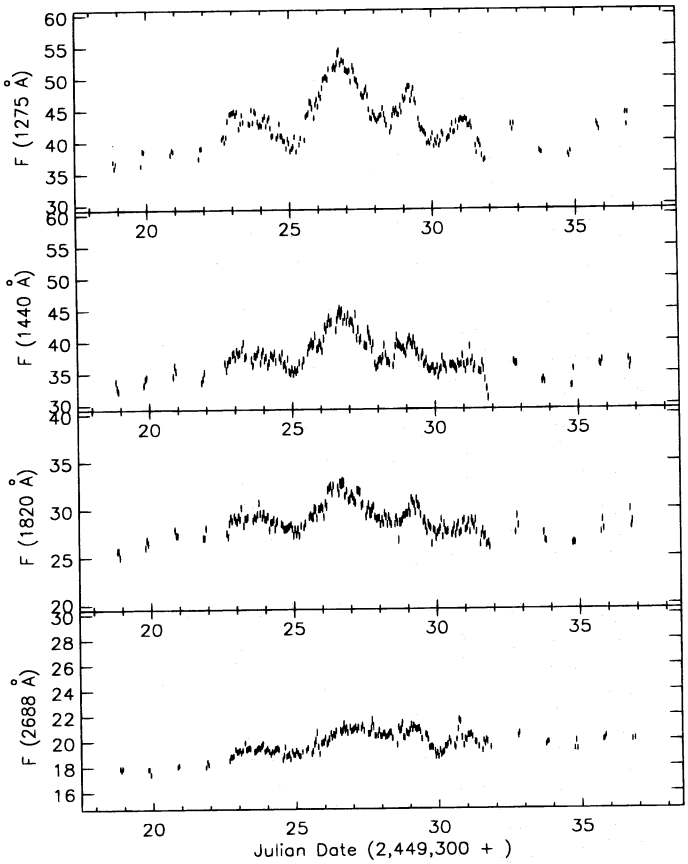

FIG. 4.—*IUE* continuum fluxes in units of 10^{-14} ergs s^{-1} cm^{-2} $Å^{-1}$ as a function of Julian Date. The fluxes are at the midpoints of the error bars ($\pm 1\,\sigma$).

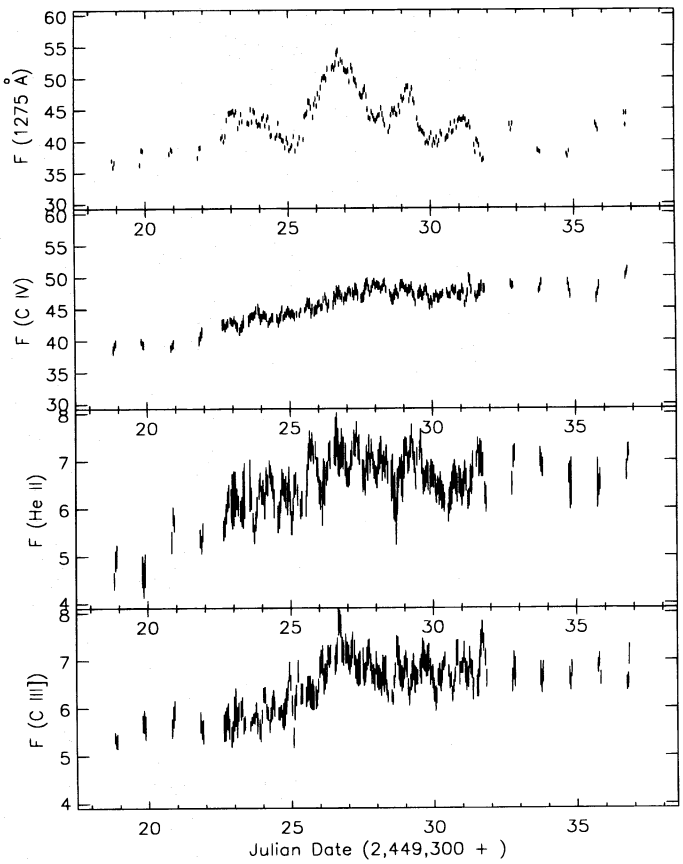

FIG. 5.—*IUE* line fluxes in units of 10^{-12} ergs s^{-1} cm^{-2} as a function of Julian Date. The fluxes are at the midpoints of the error bars ($\pm 1\,\sigma$). The continuum light curve at 1275 Å is repeated in the top panel for comparison.

of limited use, and the lags at which the cross-correlations peak are not tabulated here. A more realistic value for the C IV emission-line lag has been determined with a data set of longer duration by Clavel et al. (1990), as discussed in § 1.

5. SUMMARY AND CONCLUSIONS

We have observed the nucleus of NGC 4151 with *IUE* continuously for 9.3 days, obtaining a pair of SWP and LWP spectra every ~70 minutes, in the most intensive UV monitoring campaign to date for a Seyfert 1 galaxy. Observations were also obtained on the 4 days prior to and 5 days after the continuous-monitoring period. The *IUE* observations are part of a multiwavelength effort to study the short-timescale (hours to days) variations of NGC 4151, which have not been well characterized in the past for any Seyfert 1 galaxy.

During the monitoring period, significant variations were detected in the fluxes of the continuum bands and the emission-line features. For the continuous-monitoring period, there are four well-defined "events" in the UV continuum light curves whereas the light curves for the strong emission lines are very different, primarily showing a slow rise followed by a shallow dip. Measurement and cross-correlation of the light curves allow us to draw some important conclusions:

1. The UV continuum of NGC 4151 can vary significantly on very short timescales, going through an "event" (i.e., a significant local maximum preceded and followed by local minima) in only 2–3 days. The amplitudes of the events in this case are small compared to those found in NGC 4151 over longer timescales (Clavel et al. 1990) but are large compared to the *IUE* errors, demonstrating the feasibility and importance of continuous monitoring of AGNs in the UV.

2. The relative amplitudes of the continuum variations decrease with increasing wavelength: the ratios of largest to smallest flux value over the 18 day monitoring period are $R_{max} = 1.51$, 1.45, 1.31, and 1.24 at $\lambda = 1275$, 1440, 1820, and 2688 Å, respectively. This behavior has also been seen in the monitoring campaigns on NGC 5548 (Clavel et al. 1991; Korista et al. 1995) and NGC 3783 (Reichert et al. 1994) on longer timescales.

3. The continuum variations in all of the UV bands are *simultaneous* to within ±0.15 days (see Paper IV). This is an important and very strict constraint compared to the upper limits on UV continuum lags obtained for NGC 5548 ($\Delta t_{peak} \leq 4$ days, Clavel et al. 1991; $\Delta t_{peak} \leq 1$ day, Korista et al. 1995) and NGC 3783 ($\Delta t_{peak} \leq 4$ days, Reichert et al. 1994).

4. The emission-line variations of NGC 4151 are not always well correlated with the continuum variations over short periods of time (days or less). The apparent reason for the dissimilar continuum and emission-line light curves from our observations is the relatively short timescale for continuum variations compared to the response times of the emission lines. Consequently, cross-correlations are not very useful tools in this case; better tools (e.g., techniques

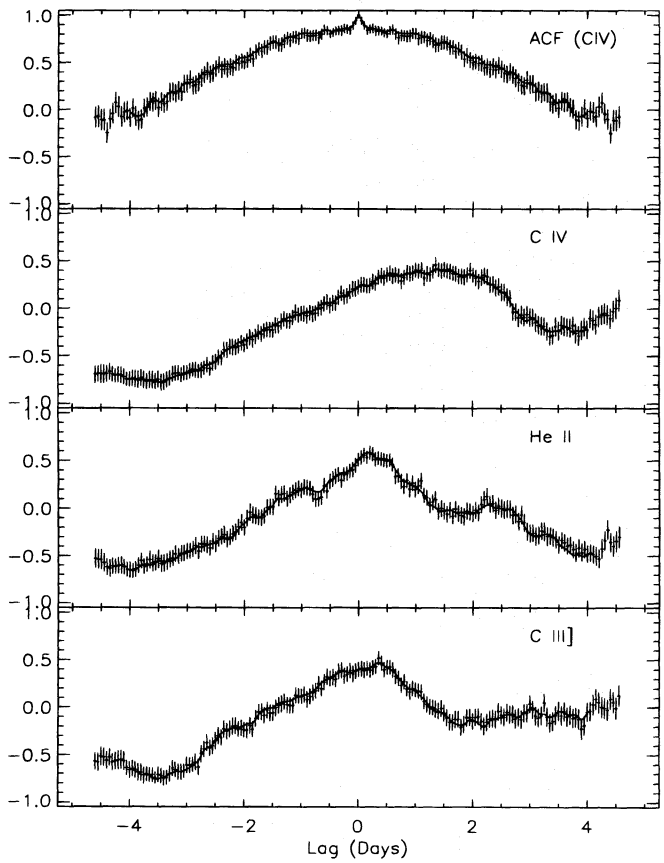

FIG. 6.—Cross-correlation of the C IV line with itself (ACF) and cross-correlation of the 1275 Å continuum band with the emission lines for the continuous data set. The CCF is given by the smooth line, and the DCF is given by the plotted points and error bars.

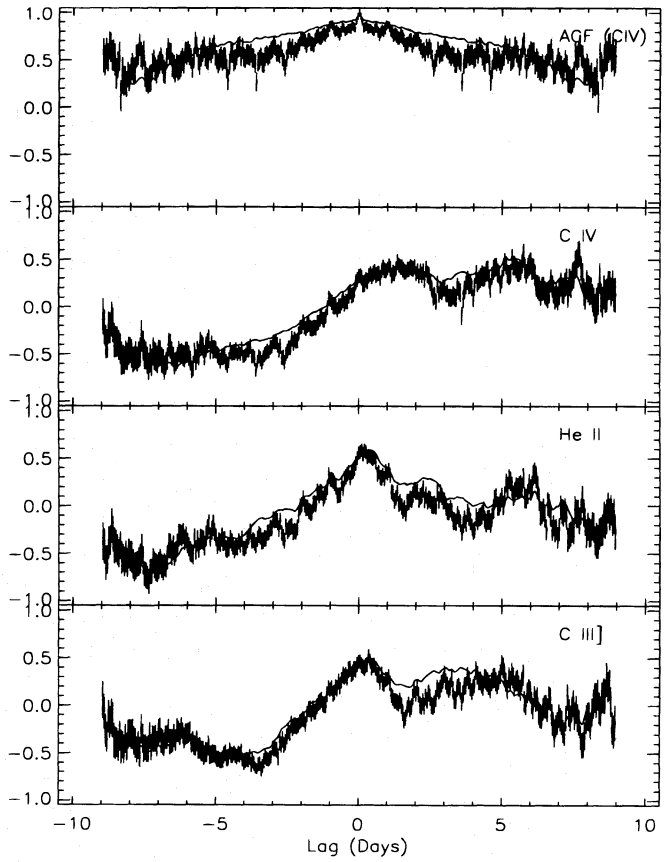

FIG. 7.—Same as Fig. 6, but for the entire data set

for determining the transfer function), longer trains of data, or both are required.

We are very grateful to the staff members of the Goddard and VILSPA *IUE* observatories for their assistance in scheduling and executing these demanding monitoring programs. We also wish to thank our many colleagues, including those on the *IUE* peer-review committees, for their support of these programs. We gratefully acknowledge financial support of this particular program through an ADP grant (NASA P.O. S-30917-F) to Computer Sciences Corporation.

REFERENCES

Ayres, T. 1993, PASP, 105, 538
Bevington, P. R. 1969, Data Reduction and Error Analysis for the Physical Sciences (New York: McGraw Hill)
Bromage, G. E., et al. 1985, MNRAS, 215, 1
Burstein, D., & Heiles, C. 1982, AJ, 87, 1165
Carini, M., & Weinstein, D. 1992, *IUE* NASA Newsl., No. 49, 5
Clavel, J., et al. 1987, ApJ, 321, 251
———. 1990, MNRAS, 246, 668
———. 1992, ApJ, 393, 113
———. 1991, ApJ, 366, 64
Collin-Souffrin, S. 1991, A&A, 249, 344
Courvoisier, T. J.-L., & Clavel, J. 1991, A&A, 248, 349
Dietrich, M., et al. 1993, ApJ, 408, 416
Edelson, R. A., et al. 1996, ApJ, 470, 364 (Paper IV)
Edelson, R. A., & Krolik, J. H. 1988, ApJ, 333, 646
Edelson, R. A., et al. 1995, ApJ, 438, 120
Evans, I. N., Tsvetanov, Z., Kriss, G. A., Ford, H. C., Caganoff, S., & Koratkar, A. P. 1993, ApJ, 417, 82
Ferland, G. J., & Mushotzky, R. F. 1982, ApJ, 262, 564
Gaskell, C. M., Koratkar, A. P., & Sparke, L. S. 1989, in IAU Symp. 134, Active Galactic Nuclei, ed. D. E. Osterbrock & J. S. Miller (Dordrecht: Kluwer), 93
Gaskell, C. M., & Peterson, B. M. 1987, ApJS, 65, 1
Gaskell, C. M., & Sparke, L. S. 1986, ApJ, 305, 175
Holt, S. S., Mushotzky, R. F., Becker, R. H., Boldt, E. A., Serlemitsos, P. J., Szymkowiak, A. E., & White, N. E. 1980, ApJ, 241, L13
James, F., & Roos, M. 1975, Comput. Phys. Commun., 10, 343
Johnston, K. J., Elvis, M., Kjer, D., & Shen, B. S. P. 1982, ApJ, 262, 61
Kaspi, S., et al. 1996, ApJ, 470, 336 (Paper II)
Kinney, A. L., Bohlin, R. C., & Neill, J. D. 1991, PASP, 103, 694
Korista, K. T., et al. 1995, ApJS, 97, 285
Kriss, G. A., et al. 1992, ApJ, 392, 485
Krolik, J. H., Horne, K., Kallman, T. R., Malkan, M. A., Edelson, R. A., & Kriss, G. A. 1991, ApJ, 371, 541
Maoz, D., et al. 1991, AJ, 367, 493
Osterbrock, D. E., & Koski, A. T. 1976, MNRAS, 176, 61P
Penston, M. V., et al. 1981, MNRAS, 196, 857
Penton, S. V., et al. 1996, in preparation
Perola, G. C., et al. 1982, MNRAS, 200, 293
Peterson, B. M. 1993, PASP, 105, 247
Peterson, B. M., et al. 1992, ApJ, 392, 470
Peterson, B. M., & Cota, S. A. 1988, ApJ, 330, 111
Peterson, B. M., et al. 1991, ApJ, 368, 119
———. 1994, ApJ, 425, 622
Reichert, G. A., et al. 1994, ApJ, 425, 582
Savage, B. D., & Mathis, J. S. 1979, ARA&A, 17, 73
Shakura, R. I., & Sunyaev, R. A. 1973, A&A, 24, 337
Simkin, S. M. 1975, ApJ, 200, 567
Stark, A. A., Gammie, C. F., Wilson, R. W., Bally, J., Linke, R. A., Heiles, C., & Hurwitz, M. 1992, ApJS, 79, 77
Stirpe, G. M., et al. 1994, ApJ, 425, 609
Ulrich, M.-H., et al. 1985, Nature, 313, 747
Ulrich, M.-H., Boksenberg, A., Bromage, G. E., Clavel, J., Elvius, A., Penston, M. V., Perola, G. C., & Snidjers, M. A. J. 1991, ApJ, 382, 483
Urry, C. M., et al. 1993, ApJ, 411, 614
Warwick, R. S., et al. 1996, ApJ, 470, 349 (Paper III)
Weaver, K. A., et al. 1994a, ApJ, 423, 621
Weaver, K., Yaqoob, T., Holt, S. S., Mushotzky, R. F., Matsuoka, M., & Yamauchi, M. 1994b, ApJ, 436, L27
White, R. J., & Peterson, B. M. 1994, ApJ, 106, 879
Wilson, A. S., & Ulvestad, J. S. 1982, ApJ, 263, 576
Yaqoob, T., Warwick, R., & Pounds, K. 1989, MNRAS, 236, 153